



Dalton  
Transactions

**Strategies for Breaking Molecular Scaling Relationships for  
the Electrochemical CO<sub>2</sub> Reduction Reaction**

Journal:	<i>Dalton Transactions</i>
Manuscript ID	DT-PER-02-2022-000333.R1
Article Type:	Perspective
Date Submitted by the Author:	18-Mar-2022
Complete List of Authors:	Nie, Weixuan; University of Michigan, Department of Chemistry McCrary, Charles; University of Michigan, Department of Chemistry; University of Michigan, Macromolecular Science & Engineering Program

SCHOLARONE™  
Manuscripts

## Strategies for Breaking Molecular Scaling Relationships for the Electrochemical CO<sub>2</sub> Reduction Reaction

Weixuan Nie<sup>a,†\*</sup> and Charles C. L. McCrory<sup>a,b\*</sup>

<sup>a</sup>Department of Chemistry, University of Michigan, Ann Arbor, Michigan, 48109-1055, United States.

<sup>b</sup> Macromolecular Science and Engineering Program, University of Michigan, Ann Arbor, Michigan, 48109-1055, United States.

<sup>†</sup>Current Address: Division of Chemistry and Chemical Engineering, California Institute of Technology, Pasadena, California, 91125-1100, United States.

\*Corresponding authors. E-mail: [niewx@umich.edu](mailto:niewx@umich.edu), [cmccrory@umich.edu](mailto:cmccrory@umich.edu)

### ORCID:

McCrory: ORCID: 0000-0001-9039-7192, Twitter: @McCroryLab

Nie: ORCID: 0000-0003-2094-6840, Twitter: @Weixuan\_Nie

### Abstract

The electrocatalytic CO<sub>2</sub> reduction reaction (CO<sub>2</sub>RR) is a promising strategy for converting CO<sub>2</sub> to fuels and value-added chemicals using renewable energy sources. Molecular electrocatalysts show promise for the selective conversion of CO<sub>2</sub> to single products with catalytic activity that can be tuned through synthetic structure modifications. However, for the CO<sub>2</sub>RR by traditional molecular catalysts, beneficial decreases in overpotentials are usually correlated with detrimental decreases in catalytic activity. This correlation is sometimes referred to as a “*molecular scaling relationship*.” Overcoming this inverse correlation between activity and effective overpotential remains a challenge when designing new, efficient molecular catalyst systems. In this perspective, we discuss some of the concepts that give rise to the *molecular scaling relationships* in the CO<sub>2</sub>RR by molecular catalysts. We then provide an overview of some reported strategies from the last decade for breaking these scaling relationships. We end by discussing strategies and progress in our own research designing efficient molecular catalysts with redox-active ligands that show high activity at low effective overpotentials for the CO<sub>2</sub>RR.

### 1. Introduction

In the last few decades, the electrocatalytic CO<sub>2</sub> reduction reaction (CO<sub>2</sub>RR) using renewable electricity generated from intermittent energy sources (e.g. solar and wind energy) has attracted increasing attention as a promising strategy for converting CO<sub>2</sub>, an industrial waste product and environmental contaminant, into solar fuels and other value-added products.<sup>1-5</sup> CO<sub>2</sub> can be reduced to variable products via different multi-electron, proton-coupled pathways. Several selected electrochemical CO<sub>2</sub> reduction processes are listed in **Table 1** with the corresponding standard redox potential  $E^0$  and standard Gibbs free energy change  $\Delta G^0$  for the reaction in aqueous solutions under standard conditions (1 atm CO<sub>2</sub>, pH 0, and 25°C).<sup>6-10</sup> Many of these multi-electron, proton-coupled CO<sub>2</sub> reduction pathways are relatively thermodynamically favorable, as evidenced by the negative or relatively small positive  $\Delta G^0$  values and near-zero  $E^0$  values.

**Table 1.** Selected CO<sub>2</sub>RR reactions with corresponding standard thermodynamic potentials  $E^0$  (V vs. SHE) and standard Gibbs free energy changes  $\Delta G^0$  for the reactions as written in aqueous solutions under standard conditions (pH = 0, 1 atm CO<sub>2</sub>, 25 °C).

Reaction Process	Major Product	$E^0$ / V	$\Delta G^0$ / kJ
$\text{CO}_2(g) + 2 \text{H}^+(aq) + 2 e^- \rightleftharpoons \text{HCOOH}(l)$	Formic acid (HCOOH)	-0.25	48.2
$\text{CO}_2(g) + 2 \text{H}^+(aq) + 2 e^- \rightleftharpoons \text{CO}(g) + \text{H}_2\text{O}(l)$	Carbon Monoxide (CO)	-0.11	21.2
$\text{CO}_2(g) + 4 \text{H}^+(aq) + 4 e^- \rightleftharpoons \text{CH}_2\text{O}(l) + \text{H}_2\text{O}(l)$	Formaldehyde (CH <sub>2</sub> O)	-0.07	27.0
$\text{CO}_2(g) + 6 \text{H}^+(aq) + 6 e^- \rightleftharpoons \text{CH}_3\text{OH}(l) + \text{H}_2\text{O}(l)$	Methanol (CH <sub>3</sub> OH)	0.02	$\Delta G^0 = -nFE^0$ -11.6
$\text{CO}_2(g) + 8 \text{H}^+(aq) + 8 e^- \rightleftharpoons \text{CH}_4(g) + 2 \text{H}_2\text{O}(l)$	Methane (CH <sub>4</sub> )	0.17	-131.2
$\text{CO}_2(g) + 12 \text{H}^+(aq) + 12 e^- \rightleftharpoons \text{CH}_3\text{CH}_2\text{OH}(l) + 3 \text{H}_2\text{O}(l)$	Ethanol (CH <sub>3</sub> CH <sub>2</sub> OH)	0.08	-92.6
$\text{CO}_2(g) + 12 \text{H}^+(aq) + 12 e^- \rightleftharpoons \text{CH}_2\text{CH}_2(g) + 4 \text{H}_2\text{O}(l)$	Ethylene (CH <sub>2</sub> CH <sub>2</sub> )	0.06	-69.5
<hr/>			
$2 \text{H}^+ + 2 e^- \rightleftharpoons \text{H}_2(g)$	Competitive HER Reaction	0.00	0.00

However, it is important to emphasize that the  $E^0$  and  $\Delta G^0$  values in **Table 1** only indicate the thermodynamic driving force necessary for these processes to occur at standard conditions (**Figure 1**). In practice, an additional driving force is required to overcome kinetic barriers and achieve a reasonable reaction rate for direct CO<sub>2</sub> reduction. This additional driving force manifests as an applied potential more negative than the thermodynamic potentials listed in **Table 1**. In the CO<sub>2</sub>RR, there is a particularly high kinetic energy barrier for direct and uncatalyzed CO<sub>2</sub> reduction through outer-sphere (non-bonded) electron transfer (**Figure 1**, red dashed curve).<sup>7-9, 11</sup> For example, the direct and uncatalyzed one-electron reduction of CO<sub>2</sub> to CO<sub>2</sub><sup>•-</sup> occurs at the very negative thermodynamic potential of -1.48 V vs. SHE. This

very negative thermodynamic potential is the result of the large structural reorganization energy between the linear  $\text{CO}_2$  molecule and the bent  $\text{CO}_2^{\bullet-}$  radical anion.<sup>6, 8, 12</sup> Although the radical anion intermediate can be sequentially protonated and/or dimerized to form thermodynamically more-favorable final products ( $\text{C}_2\text{O}_4^{2-}$  or  $\text{H}_2\text{C}_2\text{O}_4$ ), the steep kinetic energy barrier ( $\Delta G_1^\ddagger$ , Figure 1) and the large required thermodynamic Gibbs energy driving force ( $\Delta G^0_{1-e1}$ , Figure 1) for forming the initial free  $\text{CO}_2^{\bullet-}$  radical anion intermediate necessitate very negative potentials to initiate the reduction process. To avoid the formation of such high-energy intermediates, catalysts are used to stabilize reactive intermediates through the formation of reduced  $\text{CO}_2$ -adducts. This allows the reduction of  $\text{CO}_2$  through an inner-sphere electron transfer mechanism, resulting in lower kinetic energy barriers ( $\Delta G_2^\ddagger$ , Figure 1), smaller required thermodynamic Gibbs energy driving force ( $\Delta G^0_{2-e1}$ , Figure 1), and therefore more positive operating potentials (Figure 1, blue solid curve).<sup>9, 11, 13</sup>

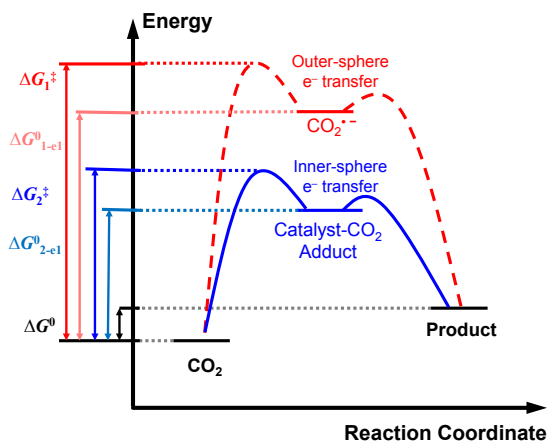


**Figure 1.** Gibbs free energy diagrams for a general electrochemical  $\text{CO}_2$  reduction process. Red dashed curve: direct and uncatalyzed  $\text{CO}_2$  reduction process that occurs through an outer-sphere electron transfer and involves the formation of a free  $\text{CO}_2^{\bullet-}$  radical anion. Blue solid curve: catalyzed  $\text{CO}_2$  reduction process that occurs through an inner-sphere electron transfer mechanism at a catalyst site involving the formation of a catalyst- $\text{CO}_2$  adduct.  $\Delta G^0$  is the thermodynamic Gibbs free energy change for the overall  $\text{CO}_2$  reduction process;  $\Delta G^0_{1-e1}$  and  $\Delta G^0_{2-e1}$  are the thermodynamic Gibbs free energy changes associated with the formation of the catalytic intermediate: either the  $\text{CO}_2^{\bullet-}$  radical anion or the catalyst- $\text{CO}_2$  adduct, respectively; and  $\Delta G_1^\ddagger$  and  $\Delta G_2^\ddagger$  are the kinetic energy barrier associated with the formation of the catalytic intermediate.

## 2. Electrocatalytic CO<sub>2</sub> Reduction

### 2.1. Electrochemical CO<sub>2</sub> Reduction by Heterogeneous Solid-State Catalysts.

In contrast to the direct CO<sub>2</sub> reduction process through the outer-sphere electron transfer on inert electrode surfaces, some solid-state materials, in particular transition metal electrodes, coordinate CO<sub>2</sub> molecules on the surface to form adsorbed CO<sub>2</sub> adducts. CO<sub>2</sub>-adduct formation is followed by or coupled with inner-sphere electron transfer at certain potentials to form different metastable reductive intermediates along various reaction pathways (**Figure 2a**).<sup>14-18</sup> These processes effectively lower the kinetic energy barrier for CO<sub>2</sub> reduction (**Figure 1**). On these heterogeneous solid-state catalyst surfaces, reasonable catalytic currents  $i_c$  for the CO<sub>2</sub>RR can be achieved at a comparatively low overpotential  $\eta$ , which is defined as the difference between the applied potential on the electrode surface  $E_{\text{electrode}}$  and the thermodynamic potential for the CO<sub>2</sub> reduction  $E_{\text{CO}_2\text{RR}}$  at a given current density (**Figure 2b**). Applying a more negative potential  $E'_{\text{electrode}}$  leads to higher overpotential  $\eta'$  (larger driving force) and lower overall kinetic energy barrier  $\Delta G^\ddagger$  for the CO<sub>2</sub> reduction, resulting in an increased magnitude catalytic current  $i_c$  (**Figure 2b**). Note that for simplicity, only the overall kinetic energy barrier for the highest-energy transition states at  $E_{\text{electrode}}$  and  $E'_{\text{electrode}}$ ,  $\Delta G^\ddagger$  and  $\Delta G'^\ddagger$  respectively, are shown in **Figure 2b**. The net effect is that catalytic cyclic voltammograms (CVs) for solid-state heterogeneous catalysts show increasing magnitude  $i_c$  as the  $E_{\text{electrode}}$  is scanned to more negative potentials (**Figure 2c**), consistent with the trend observed from the Tafel plot where current is acquired under steady state conditions at each  $E_{\text{electrode}}$  examined.<sup>19</sup>

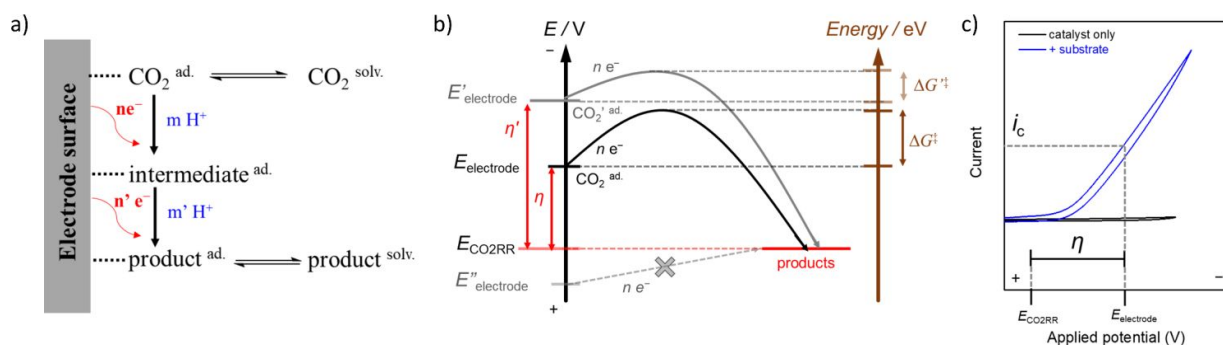


**Figure 2.** a) General mechanism for an electrochemical  $\text{CO}_2$  reduction at a heterogeneous electrode surface. b) Schematic representation of the overall electron transfer process for the electrochemical  $\text{CO}_2\text{RR}$  by a heterogeneous solid-state catalyst. For simplicity, we do not depict individual electron transfer or intermediate steps, and instead only the overall kinetic energy barrier,  $\Delta G^\ddagger$  and  $\Delta G'^{\ddagger}$  for the highest-energy transition state at  $E_{\text{electrode}}$  and  $E'_{\text{electrode}}$ , respectively, is illustrated. c) Schematic representation of cyclic voltammograms of a heterogeneous solid-state catalyst in the presence (blue curve) and absence (black curve) of the substrate  $\text{CO}_2$ .

In the last decade, significant effort has been devoted to improving the mechanistic understanding of the catalytic processes at solid-state catalysts for the  $\text{CO}_2\text{RR}$ .<sup>14-18, 20-26</sup> Many experimental and computational studies show that the lack of product selectivity in the  $\text{CO}_2\text{RR}$  remains a challenge for the solid-state catalysts despite the good activity achieved at low overpotentials.<sup>14-18, 27</sup> This selectivity challenge exists because the most active solid-state electrode surfaces can adsorb many different reductive  $\text{CO}_2$  intermediates. The competition among these binding species on the catalytic electrode surface is a key factor governing the final distribution of reduction products.<sup>27</sup> For example, Au and Ag catalysts mainly reduce  $\text{CO}_2$  to CO but still suffer from competitive  $\text{H}_2$  formation in protic solutions,<sup>16-18</sup> while Cu electrode generates up to 16 C-based products including multi-carbon products in aqueous solutions.<sup>14-16</sup>

In addition to the chemical composition of electrodes, the different surface morphology of the same material also has a significant effect on the product distribution for the  $\text{CO}_2\text{RR}$ .<sup>8</sup> In general, solid-state catalyst materials with a higher density of low-coordination sites such as edges, steps, defects, and specific exposed crystal facets exhibit higher activity and selectivity for specific  $\text{CO}_2\text{RR}$  products.<sup>28-31</sup> Based on these experimental discoveries, recent advances in solid-state catalyst design, including the use of nanostructured and mesoporous catalyst surfaces and composite electrode materials, show increased

selectivity for specific products.<sup>20-26</sup> However unpredictable structural changes of these materials *operando* at varying applied electrode potentials raise another issue of potential dependent selectivity for the solid-state catalysts.<sup>5, 32, 33</sup>

## 2.2. Electrochemical CO<sub>2</sub> Reduction by Homogenous Molecular electrocatalysts.

In comparison to heterogeneous solid-state catalysts, homogenous molecular catalysts, in particular transition metal complexes, show significant promise for the selective conversion of CO<sub>2</sub> to single products. Instead of transferring electrons directly from the electrode surface to the adsorbed CO<sub>2</sub> molecules, the homogenous molecular catalysts act as electron shuttles between the electrode and CO<sub>2</sub> molecules (**Figure 3a**).<sup>6, 9, 13</sup> In this case, the molecular catalyst Cat is first reduced to the active species Cat<sup>n-</sup> on the electrode surface at its own redox potential  $E_{\text{cat}/2}$  in an initial electron transport event from the electrode (E<sub>1</sub> step, **Figure 3a**). This initial reduction of Cat to Cat<sup>n-</sup> initiates the catalytic cycle. The active species Cat<sup>n-</sup> then diffuses and coordinates CO<sub>2</sub> to form a CO<sub>2</sub>-adduct intermediate [Cat-CO<sub>2</sub>]<sup>n-</sup> in a chemical step (C<sub>1</sub>) with kinetic rate  $k_{\text{C1}}$  (**Figure 3a**). The metastable intermediate [Cat-CO<sub>2</sub>]<sup>n-</sup> can be further reduced (E<sub>2</sub>) on the electrode surface and/or protonated (C<sub>2</sub>) by the proton source in the solution to generate the final product. Upon product release, the molecular catalyst Cat is regenerated, allowing it to reenter the catalytic cycle. In order for efficient homogeneous molecular electrocatalysis, both the electron transfer and chemical steps should be sufficiently fast such that Cat can undergo multiple catalytic cycles during its residence time within the electrode diffusion layer.

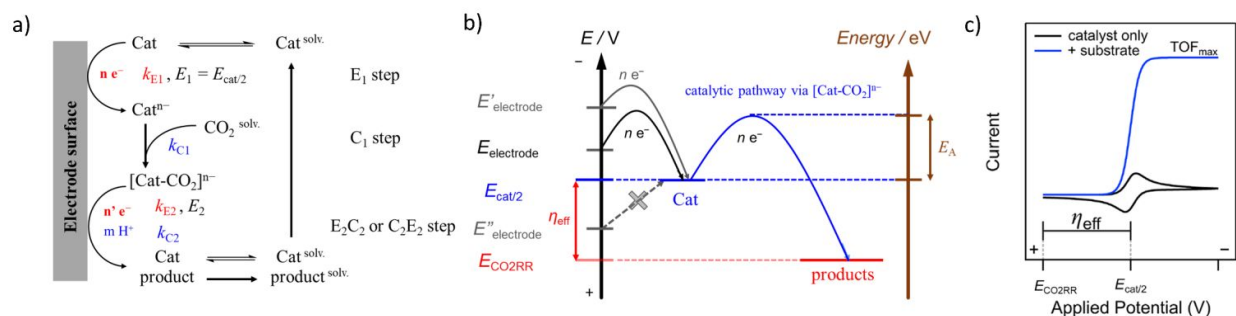


**Figure 3.** a) General mechanistic scheme for electrochemical  $CO_2$  reduction by a homogeneous molecular catalyst. b) Schematic representation of the overall electron transfer process for the electrochemical  $CO_2RR$  by a homogenous molecular catalyst via the formation of  $[Cat-CO_2]^{n-}$ . For simplicity, only the overall kinetic energy barrier  $E_A$  for the highest-energy transition state is depicted. c) Schematic representation of cyclic voltammograms of a homogenous molecular catalyst for the  $CO_2RR$  in the presence (blue curve) and absence (black curve) of the substrate  $CO_2$ , adapted with permission from *Acc. Chem. Res.* **2020**, 53, 5, 1056–1065.<sup>34</sup> Copyright 2020 American Chemical Society.

In the process of the homogenous catalysis discussed above, the redox potential  $E_{cat/2}$  of the molecular catalyst should be more negative than the thermodynamic  $CO_2RR$  potential  $E_{CO2RR}$ , providing a thermodynamic driving force for the electron transfer from the molecular catalyst to the  $CO_2$  molecule (**Figure 3b**). The difference between  $E_{cat/2}$  and  $E_{CO2RR}$  is referred to as the effective overpotential  $\eta_{eff}$  for the catalytic reaction for a given molecular catalyst.<sup>6, 9, 13, 34</sup> In contrast to the scenario of heterogenous solid-state catalysts (**Figure 2**), the effective overpotential  $\eta_{eff}$  for the  $CO_2RR$  by molecular catalysts does not change as a function of the applied electrode potential  $E_{electrode}$ , because both potential  $E_{CO2RR}$  and  $E_{cat/2}$  are fixed during the catalytic process.<sup>6, 9, 13</sup> More negative  $E'_{electrode}$  can facilitate the redox activation/conversion of the molecular catalyst and the intermediate ( $E_1$  and  $E_2$  step), but has no influence on the  $CO_2$  bonding and protonation steps ( $C_1$  and  $C_2$  steps) in the catalytic cycle. The chemical steps  $C_1$  and  $C_2$  are related only to the intrinsic electronic features of the catalysts, which are independent of the electrode potential. Therefore, in most cases where chemical steps are rate-determining and if the system is under kinetically-limiting conditions, the catalytic current will reach a maximum plateau instead of increasing as the electrode potential is driven more negative under ideally kinetic conditions (**Figure 3c**).<sup>11,</sup>

<sup>35</sup> The maximum catalytic turnover frequency ( $\text{TOF}_{\text{max}}$ ) can be estimated from the plateaued catalytic current. This characteristic of the catalytic CVs of molecular catalysts indicates that the maximum catalytic activity for the  $\text{CO}_2\text{RR}$  is modulated by the intrinsic catalytic ability of the molecular catalyst rather than by the electron transfer at the electrode interface.<sup>11, 35</sup>

Unlike solid-state catalysts that can support various reactive intermediates at different binding sites, molecular catalysts typically provide a single type of coordination environment to bind  $\text{CO}_2$  at the metal center to form  $\text{CO}_2$ -adduct intermediates with specific coordination modes. These specific intermediates structure can be further reduced and/or protonated to generate single products (usually  $\text{CO}$  or  $\text{HCOOH}$ ).<sup>6, 7, 11</sup> In addition to having improved selectivity for the  $\text{CO}_2\text{RR}$ , molecule catalysts have tunable ligand scaffolds that allow for control of the metal complexes' electronic properties and the coordination sphere environments. This ligand tunability provides opportunities to design and develop efficient catalyst systems with both high activity and excellent selectivity for the  $\text{CO}_2\text{RR}$  through rational design and modification of the ligand structure.<sup>36-43</sup>

### 3. Scaling Relationships for Molecular Catalysts

For homogeneous molecular catalysts for the  $\text{CO}_2\text{RR}$ , the kinetic reactivity ( $\text{TOF}_{\text{max}}$ ) and the effective overpotential ( $\eta_{\text{eff}}$ ) can be estimated from electrochemical measurements. Analyzing the correlation between  $\text{TOF}_{\text{max}}$  and  $\eta_{\text{eff}}$  for the  $\text{CO}_2\text{RR}$  by molecular catalysts with different structural features allows for the derivation of structure/activity relationships. Understanding such relationships is essential for developing more efficient next-generation molecular catalysts.

Ideally, the most efficient molecular catalysts can reduce  $\text{CO}_2$  with the highest  $\text{TOF}_{\text{max}}$  but at the lowest  $\eta_{\text{eff}}$  (the top left area of **Figure 4a**).<sup>34, 44</sup> However, for most electrocatalytic reactions at molecular catalysts including  $\text{H}_2$  evolution,<sup>45-47</sup>  $\text{O}_2$  reduction,<sup>48</sup> and  $\text{CO}_2$  reduction,<sup>49-51</sup> beneficial decreases in  $\eta_{\text{eff}}$  are typically correlated with detrimental decreases in  $\text{TOF}_{\text{max}}$ . This general trend is often referred to as a “*molecular scaling relationship*” (**Figure 4a**).<sup>34</sup> The main reason for this molecular scaling relationship is that both the kinetic reactivity ( $\text{TOF}_{\text{max}}$ ) and the effective overpotential ( $\eta_{\text{eff}}$ ) scale with a catalyst's metal site's ability to

coordinate and activate the substrate, which in turn is often correlated with the metal site nucleophilicity (**Figure 4b**).<sup>52, 53</sup> This is conceptually comparable to the general scaling relationships seen in heterogeneous solid-state catalyst systems, where electrocatalytic activity is correlated to the electrode potential because they both scale with the adsorption energy of the CO<sub>2</sub>RR intermediates on the electrode surface.<sup>54</sup>

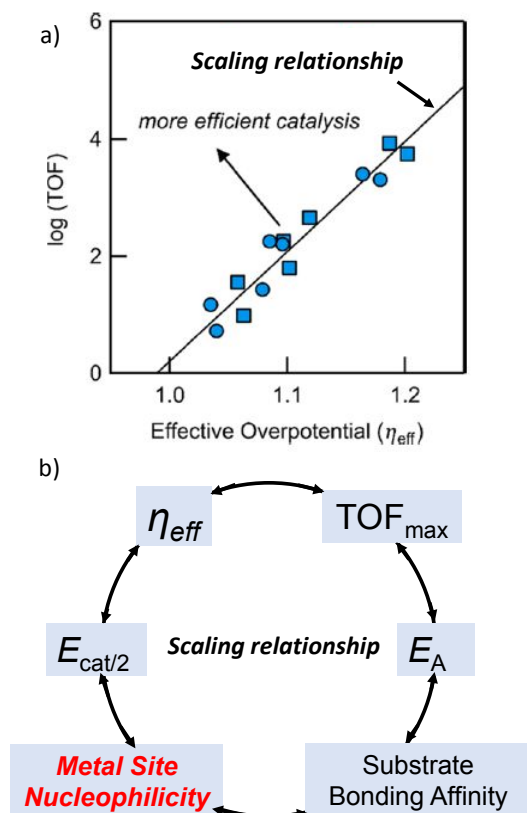


**Figure 4.** a) The “scaling relationship” between TOF and  $\eta_{\text{eff}}$  for molecular catalysts. Adapted with permission from *J. Am. Chem. Soc.* **2017**, *139*, 11000-11003.<sup>44</sup> <https://pubs.acs.org/doi/abs/10.1021/jacs.7b05642>. Copyright 2017 American Chemical Society. Further permissions related to the material excerpted should be directed to the ACS. b) thermodynamic parameters ( $\eta_{\text{eff}}$  and  $E_{\text{cat}/2}$ ) and kinetic parameters ( $E_{\text{A}}$  and  $\text{TOF}_{\text{max}}$ ) scale up with the metal site nucleophilicity to bond and activate CO<sub>2</sub> molecules.

For typical molecular catalysts, CO<sub>2</sub> coordination and reduction immediately follows a metal-based reduction event. Therefore, the activity of the catalyst is related to the ability of the reduced metal center to coordinate and activate CO<sub>2</sub>.<sup>52, 55</sup> Modifying the molecular catalyst’s structure can shift the redox

potential  $E_{\text{cat}/2}$  of the metal center positive to  $E_{\text{cat}/2}'$ , decreasing the effective overpotential ( $\eta_{\text{eff}}$ ) for the CO<sub>2</sub>RR (**Figure 5a**). However, the more positive  $E_{\text{cat}/2}'$  leads to a decrease in the nucleophilicity of the metal site, limiting the complex's ability to coordinate and activate CO<sub>2</sub>, thus increasing the kinetic activation energy  $E_A'$  for the overall catalytic process (**Figure 5a**).<sup>56-58</sup> As a result, although the corresponding catalytic onset occurs with a lower effective overpotential  $\eta_{\text{eff}}$ , the maximum plateau current and activity (TOF<sub>max</sub>') is decreased in the catalytic CV (**Figure 5b**).

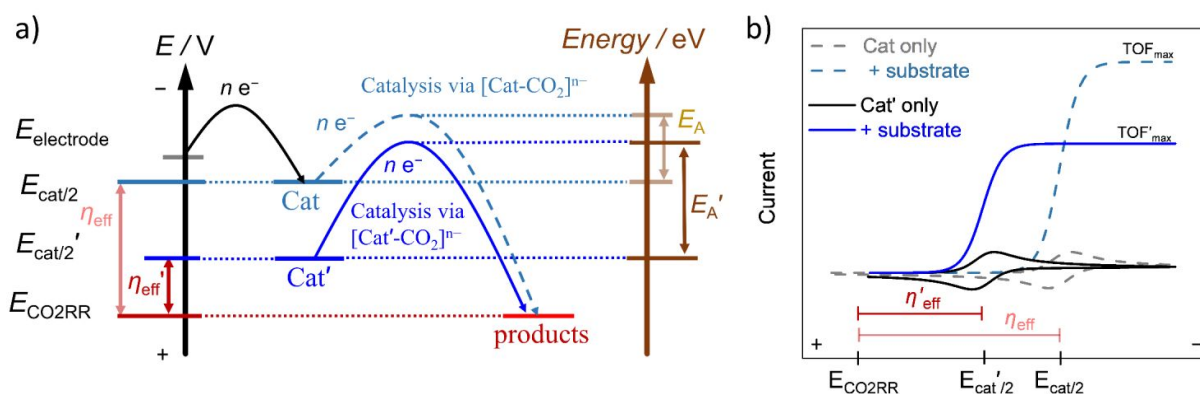


**Figure 5.** a) Shifting  $E_{\text{cat}/2}$  positive to  $E_{\text{cat}/2}'$  decreases the magnitude of  $\eta_{\text{eff}}$  to  $\eta_{\text{eff}}'$ , but also increase  $E_A$  to  $E_A'$ . For simplicity, only the overall kinetic energy barrier  $E_A$  and  $E_A'$  for the highest-energy transition states for the catalysts Cat and Cat' are depicted. b) The result is a positive shift in the onset potential for the CO<sub>2</sub>RR, but a decrease in the maximum activity for the CO<sub>2</sub>RR. This correlation between decreasing  $\eta_{\text{eff}}$  and decreasing TOF<sub>max</sub> is often referred to as a typical *molecular scaling relationship*.

Nevertheless, elucidating the correlation between thermodynamic  $\eta_{\text{eff}}$  and kinetic TOF<sub>max</sub> for molecular catalysts is complicated because many experimental factors in practical scenarios influence these two metrics.<sup>34</sup> For instance,  $\eta_{\text{eff}}$  varies with the change of either  $E_{\text{cat}/2}$  or  $E_{\text{CO2RR}}$ , and  $E_{\text{CO2RR}}$  varies in different solvents based on the buffer  $\text{p}K_a$  of the added electrolyte and proton sources.<sup>59, 60</sup> In addition, molecular catalysts comprised of different metal centers (early or late transition metals)<sup>38</sup> and ligand scaffolds (porphyrin, phthalocyanine, bipyridine, pyridyldiimine, etc.)<sup>37, 41, 61, 62</sup> have varying electronic structures and catalytic abilities that influence the kinetic parameter TOF<sub>max</sub>. Despite these complications, several emerging studies have been reported in the last few years that have attempted to identify the parameters

that effect the scaling relationships for molecular catalysts,<sup>44, 48, 63</sup> and to determine useful strategies to break these molecular scaling relationships.<sup>44, 45, 48, 64-73</sup> In the next sections, strategies for breaking molecular scaling relationships reported in the last decade will be summarized and discussed. This discussion will be followed by an overview of the progress from our laboratory in designing molecular catalysts with redox-active ligands to break molecular scaling relationships as efficient molecular catalyst systems for the CO<sub>2</sub>RR.

#### 4. Strategies for Breaking Molecular Scaling Relationships

The development of sophisticated benchmarking procedures for homogeneous molecular catalysts in the last few years<sup>11, 74-79</sup> has resulted in numerous investigations and discussions regarding the structure-activity relationships for molecular catalysts for the CO<sub>2</sub>RR.<sup>34, 49, 55, 62, 63, 80</sup> These studies have demonstrated that the typical *molecular scaling relationship*—the trade-off between  $\eta_{\text{eff}}$  and TOF<sub>max</sub>—is one of the main obstacles for designing and developing more efficient molecular catalysts. For typical molecular catalysts, the *catalytic onset for the CO<sub>2</sub>RR is preceded by the reduction of the metal center*. In such systems, the activity of the catalyst is correlated with the ability of the reduced metal center to coordinate CO<sub>2</sub> to form CO<sub>2</sub>-adduct intermediates (**Figure 4b**).<sup>52, 55</sup> Shifting the redox potential ( $E_{\text{cat}/2}$ ) of these typical molecular catalysts more positive lowers  $\eta_{\text{eff}}$ , but also decreases the nucleophilicity of the reduced metal center and decreases the metal center's ability to bind CO<sub>2</sub>.<sup>52, 55</sup> However, if the CO<sub>2</sub>-adduct intermediate can be effectively stabilized through substituent effects introduced into the catalyst's structure, it is possible to maintain or even enhance the catalytic activity for the CO<sub>2</sub>RR at lower  $\eta_{\text{eff}}$ , overcoming the detrimental effect of decreased nucleophilicity of the metal center on the catalytic activity. Three strategies have been emerged in the past several years to stabilize CO<sub>2</sub>-adduct intermediates and break *molecular scaling relationships* through ligand and catalyst modifications (**Figure 6**).<sup>44, 45, 48, 64-73</sup> In this section, we will introduce and discuss these strategies in detail.

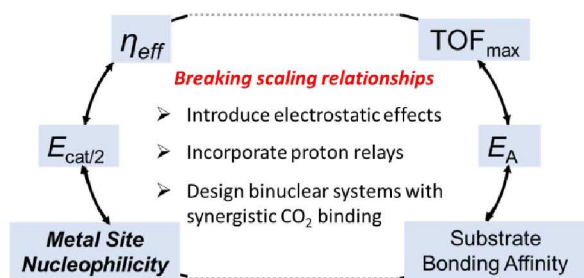


**Figure 6.** Three strategies for breaking molecular scaling relationships for the CO<sub>2</sub>RR.

#### 4.1. Introducing Intramolecular Electrostatic Effects into the Structure of Metal Complexes.

Modifying the structures of molecular catalysts by incorporating inductive effects into the ligand scaffold does not generally break molecular scaling relationships between  $\eta_{\text{eff}}$  and  $\text{TOF}_{\text{max}}$ . This is because for most molecular catalysts where catalytic onset is preceded by the reduction of the metal center, incorporating electron-withdrawing functional groups into the catalyst structure shifts the redox potential  $E_{\text{cat}/2}$  more positive. This positive shift in  $E_{\text{cat}/2}$  results in a decrease in the nucleophilicity of the metal center, and thus lower  $\text{TOF}_{\text{max}}$ . For example, in the case of the CO<sub>2</sub>RR by a series of Fe(TPP) complexes modified with pentafluorophenyl groups (**Figure 7**, FeTPP, FeF5TPP, FeF10TPP and FeF20TPP), incorporating more electron-withdrawing pentafluorophenyl groups into the structure leads to a beneficial decrease in  $E_{\text{cat}/2}$  (labeled  $E_{\text{cat}}^0$ ), but also a detrimental decrease in  $\text{TOF}_{\text{max}}$ .<sup>49</sup> However, when cationic trimethylanilinium (TMA) groups are incorporated into the FeTPP structure, notable deviations from a typical molecular scaling relationship is observed (**Figure 7**, Fe-*p*-TMA, Fe-*o*-TMA).<sup>73</sup> Fe-*p*-TMA catalyzes the reduction of CO<sub>2</sub> with greater than one order of magnitude higher activity ( $\log(\text{TOF})$ ) compared to FeF10TPP at the same overpotential  $\eta$  (**Figure 7**).<sup>73</sup> This increase in CO<sub>2</sub>RR activity of Fe-*p*-TMA is attributed to the through-space Coulombic stabilization of the reduced Fe-CO<sub>2</sub> adduct structure by the positively-charged TMA groups.<sup>73</sup> We refer to this electric field stabilization of reduced intermediates as an *intramolecular electrostatic effect*. In contrast, Fe-*p*-PSULF contains four anionic sulfonate groups at the *para* positions of TPP phenyl rings. Accordingly, Fe-*p*-PSULF catalyzes the reduction of CO<sub>2</sub> at lower activity compared to FeF10TPP at the same overpotential  $\eta$  due to Coulombic destabilization of the CO<sub>2</sub>-adduct by the negatively charged

sulfonate groups.<sup>73</sup> Moving the cationic trimethylanilinium groups to the *ortho* position of TPP phenyl rings results in the most efficient catalyst of the series for the CO<sub>2</sub>RR, Fe-*o*-TMA.<sup>73</sup> The additional increased CO<sub>2</sub>RR activity of Fe-*o*-TMA compared to Fe-*p*-TMA has been attributed to the closer proximity of the cationic substituents to the CO<sub>2</sub>-binding site, enhancing the stabilization of Fe-CO<sub>2</sub> adduct via an increased intramolecular electrostatic effect.<sup>73</sup>

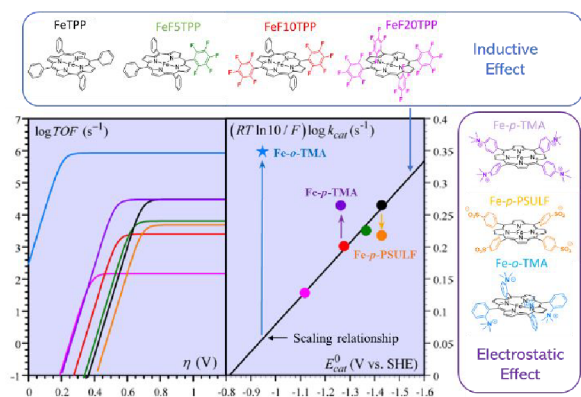


**Figure 7.** (Left) Molecular catalytic Tafel plots of logTOF vs.  $\eta$  and (Right) correlation between  $\text{TOF}_{\text{max}} = k_{\text{cat}}$  and redox potentials of the catalysts  $E_{\text{cat}}^0$  for iron tetraphenylporphyrin (TPP) complexes: FeTPP (black), FeF5TPP (green), FeF10TPP (red), FeF20TPP (magenta), Fe-*p*-TMA (purple), Fe-*p*-PSULF (orange), and Fe-*o*-TMA (blue). Adapted with permission from *J. Am. Chem. Soc.* **2016**, 138, 51, 16639–16644.<sup>73</sup> Copyright 2016 American Chemical Society.

Another approach used to introduce intramolecular electrostatic effects into molecular catalysts is to incorporate alkali and alkaline cations ( $M_2 = \text{Na}^+, \text{K}^+, \text{Ca}^{2+}, \text{Sr}^{2+}$  and  $\text{Ba}^{2+}$ ) into crown-like cavities appended to the transition metal Schiff base complexes ( $M_1 = \text{Co}^{2+}, \text{Ni}^{2+}, \text{Fe}^{2+}$ , and  $\text{Mn}^{2+}$ ) (**Figure 8a**).<sup>81-84</sup> Here, the redox-inactive  $M_2$  cations tune the potential of the redox-active  $M_1$  sites. For instance, in dicationic  $[\text{M}_1\text{M}_2]^{n+}$  complexes based on Co(salen) derivatives with incorporated  $M_2$  sites (**Figure 8b**), the  $\text{Co}^{2+/+}$  redox potential is shifted to a more positive potential compared to the parent Co(salen) complex, with the extent of potential shift correlated with the ionic size and Lewis acidity of  $M_2$ .<sup>81</sup> Similar correlations are observed for Ni, Fe and Mn-salen- $M_2$  complexes.<sup>82-84</sup> According to the results of electronic absorption, infrared spectra, and DFT calculations of these  $[\text{M}_1\text{M}_2]^{n+}$  structures, the incorporated redox-inactive  $M_2$  cations have

a negligible influence on the ordering of the molecular orbitals in the  $M_1$  transition metal. This result suggests that the positive shift in the  $M_1$  redox potential in the  $[M_1M_2]^{n+}$  complexes arises from the electrostatic field exerted by the redox inactive  $M_2$  cations, as opposed to an inductive effect of  $M_2$  cations on the electronic structure of  $M_1$  center.<sup>81-84</sup>

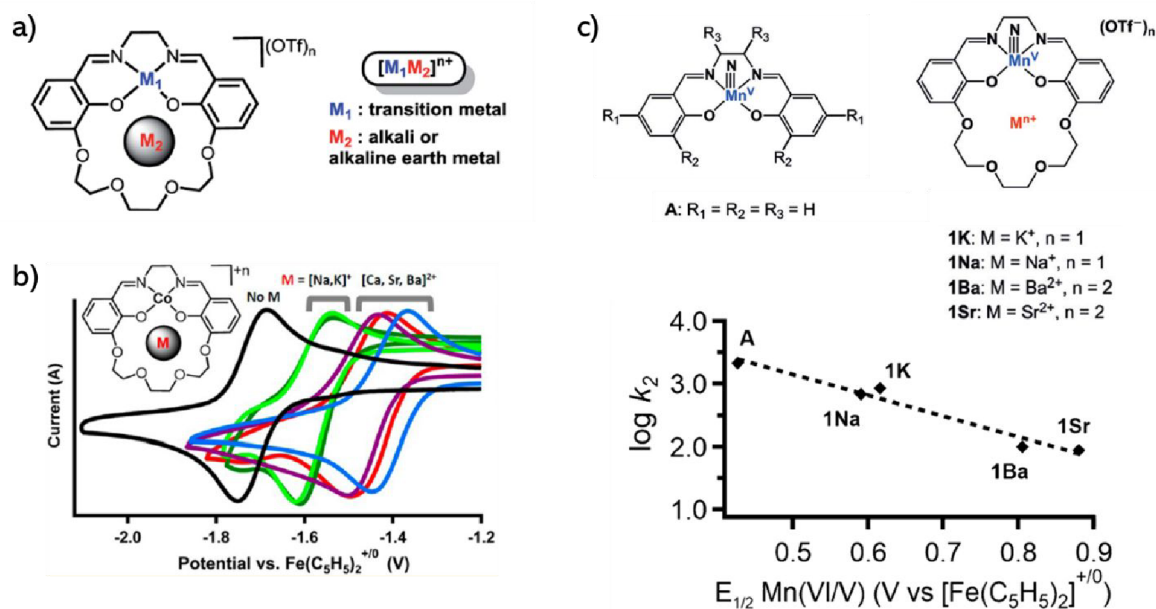


**Figure 8.** a) The structures of a series of transition metal Schiff-base complexes with alkali and alkaline cations incorporated in the crown-like cavity appended to the ligand. Adapted with permission from *Chem.Sci.*, **2019**, 10, 10135,<sup>84</sup> with permission from the Royal Society of Chemistry. b) Representative cyclic voltammograms showing the potential shift of  $Co^{2+/+}$  redox potential correlated with the ionic size and Lewis acidity of  $M_2$  for  $Co(salen)$  complexes. Adapted with permission from *Inorg. Chem.* **2017**, 56, 6, 3713–3718.<sup>81</sup> Copyright 2017 American Chemical Society. c) Top: the structures of  $Mn^V$  Schiff-base complex **A** and modified dicationic complexes with redox inactive cations incorporated **1Na**, **1K**, **1Ba** and **1Sr**; Bottom: an inverse linear scaling relationship between reaction rate ( $k_2$ ) and the redox potential of Mn sites ( $E_{1/2}(Mn^{VI/V})$ ) for **A**, **1Na**, **1K**, **1Ba** and **1Sr**. Adapted with permission from *Angew. Chem. Int. Ed.* **2018**, 57, 14037–14042,<sup>83</sup> © 2018 Wiley-VCH Verlag GmbH & Co. KGaA, Weinheim.

Although the bimetallic  $[M_1M_2]^{n+}$  complexes in **Figure 8** were not reported for the  $CO_2RR$ ,  $M_1$ -salen- $M_2$  structures have been used to break *molecular scaling relationships* in other electrochemical reactions.<sup>82, 83</sup>

In one example, Fe(salen) complexes with incorporated redox-inactive cations show increased catalytic activity for aerobic C-H oxidation at more negative potentials (lower  $\eta_{\text{eff}}$ ) compared to the parent complexes.<sup>82</sup> Another example focuses on developing stable, high-valent Mn-nitride complexes with radical character which can be used as reactants in downstream stoichiometric or catalytic reactions.<sup>83</sup> Upon electrochemical oxidation, Mn<sup>V</sup>N Schiff based complexes (**Figure 8c**, complex A) are oxidized to the desired Mn<sup>VI</sup>N complex. However, this Mn<sup>VI</sup>N complex is unstable and undergoes a fast and undesirable bimolecular coupling and degradation ( $k_2$ ) to form N<sub>2</sub> and two equivalents of the Mn<sup>III</sup> precursor complex. Introducing inductive effects to complex A results in a typical scaling relationship—as electron-withdrawing substituents are added to the ligand backbone, the potential of the Mn<sup>VI/V</sup> ( $E_{1/2}(\text{Mn}^{\text{VI/V}})$ ) couple shifts positive which destabilizes the Mn<sup>VI</sup>N and increases the rate of the undesired bimolecular coupling degradation pathway.<sup>83</sup> In contrast, incorporating redox-inactive M<sub>2</sub> cations into the structure (**Figure 8c**, complexes 1K, 1Na, 1Ba, and 1Sr) leads to an *inverse scaling relationship*—as the charge and Lewis acidity of M<sub>2</sub> increases, there is both a corresponding beneficial positive shift in the Mn<sup>VI/V</sup> redox potential, and an increase in the stability of the Mn<sup>VI</sup>N against the undesired bimolecular coupling degradation pathway. The introduction of electrostatic effects to break traditional scaling relationships in undesirable degradation reactions was proposed as a new strategy for stabilizing active reactants against bimolecular deactivation.<sup>83</sup> These examples demonstrate that the incorporation of intramolecular electrostatic effects into catalyst structures by adding secondary redox-inactive metals is an effective strategy to break typical molecular scaling relationships.

## 4.2. Incorporating Proton Relays into the Secondary Coordination Environment of the Catalysts

### 4.2.a. Incorporating Acidic Proton Relays to Increase the Local Proton Concentration Proximate to the Catalytic Active Site.

Enzymatic systems such as the Ni-Fe carbon monoxide dehydrogenase enzyme (Ni-Fe-CODH) provide biological inspiration for the design of new molecular catalyst systems that operate with high activity and product selectivity.<sup>1, 43, 85</sup> The high activity of Ni-Fe-CODH for the selective interconversion of CO<sub>2</sub> and CO

is partially attributed to the presence of histidine and lysine residues in the secondary coordination sphere of the active site that help deliver protons and stabilize reduced CO<sub>2</sub> intermediates through H-bonding interactions.<sup>1, 86</sup> To this end, many studies have explored incorporating acidic proton relays into the secondary coordination sphere of molecular catalysts to facilitate the CO<sub>2</sub>RR at faster rates at lower effective overpotentials, breaking molecular scaling relationships.<sup>1, 42</sup>

In one example, acidic phenolic hydroxyl groups were incorporated into the *ortho* and *ortho'* sites of TPP phenyl groups of the FeTPP complex to mimic the protonic secondary coordination environment found in Ni,Fe-CODH.<sup>65</sup> The resulting FeTDHPP complex operates with considerably higher activity for the CO<sub>2</sub>RR to CO compared to the parent FeTPP complex using 2.0 M H<sub>2</sub>O as the proton source.<sup>65</sup> In comparison, the analogue FeTDMPP replaces the hydroxyl groups with methoxy groups, leading to significantly decreased overall activity compared to the FeTDHPP (**Figure 9a**).<sup>65</sup> The enhanced catalytic activity of FeTDHPP is proposed to be due to increased local proton concentration associated with the proximate phenolic hydroxyl moieties. This postulate is supported by a control experiment where the FeTPP complex was able to reduce CO<sub>2</sub> to CO with equivalent activity to FeTDHPP, but only with significantly higher concentration (150 M) of PhOH added to the electrolyte as a proton source.<sup>65</sup> The net result is that, under identical conditions, FeTDHPP operates at lower overpotentials with higher activity compared to FeTPP and FeTDMPP, breaking typical molecular scaling relationships.

A similar increase in catalytic ability was observed in the study of the CO<sub>2</sub>RR by a series of iron heme-like porphyrin complexes bearing pendant arenesulfonic acid (HPDFe-3SA), guanidyl (HPDFe-Gnd) and phenolic (HPDFe-PhOH) groups in the secondary coordination sphere (**Figure 9b**).<sup>72</sup> HPDFe-PhOH shows both higher activity and lower effective overpotential for the CO<sub>2</sub>RR compared to HPDFe-Gnd using PhOH as a proton source, breaking typical molecular scaling relationships. This result is attributed to the lower pK<sub>a</sub> of the pendant phenolic hydroxyl group in HPDFe-PhOH compared to that of the pendant guanidyl group in HPDFe-Gnd. The lower pK<sub>a</sub> of the phenolic group in HPDFe-PhOH is thought to better stabilize reduced intermediates through intramolecular hydrogen-bonding effects, and enhance proton transfer to the reduced CO<sub>2</sub> adducts by increasing the effective proton concentration proximate to the active Fe site.<sup>72</sup>

Interestingly, in the example above, incorporating an even more acidic arenesulfonic acid pendant group to form HPDFe-3SA leads to lower activity compared to HPDFe-PhOH (**Figure 9b**).<sup>72</sup> HPDFe-3SA's decreased CO<sub>2</sub>RR activity is due to the DMF solvent effectively deprotonating the acidic arenesulfonic acid group, leaving an anionic pendant arenesulfonate group close to the catalyst active site. The deprotonation of the arenesulfonic acid results in an unintentional detrimental intramolecular electrostatic effect, in which the Coulombic repulsion between the negatively charged porphyrin ring and the anionic arenesulfonate group hinders the effective H-bonding interaction in the secondary coordination sphere of the reduced CO<sub>2</sub> adduct at the Fe site.<sup>72</sup> This example shows a fundamental limitation of breaking scaling relationships through incorporation of acidic proton donors—the pK<sub>a</sub> of the proton donor incorporated into the ligand scaffold must always be larger than the pK<sub>a</sub> of the solvent and proton source.

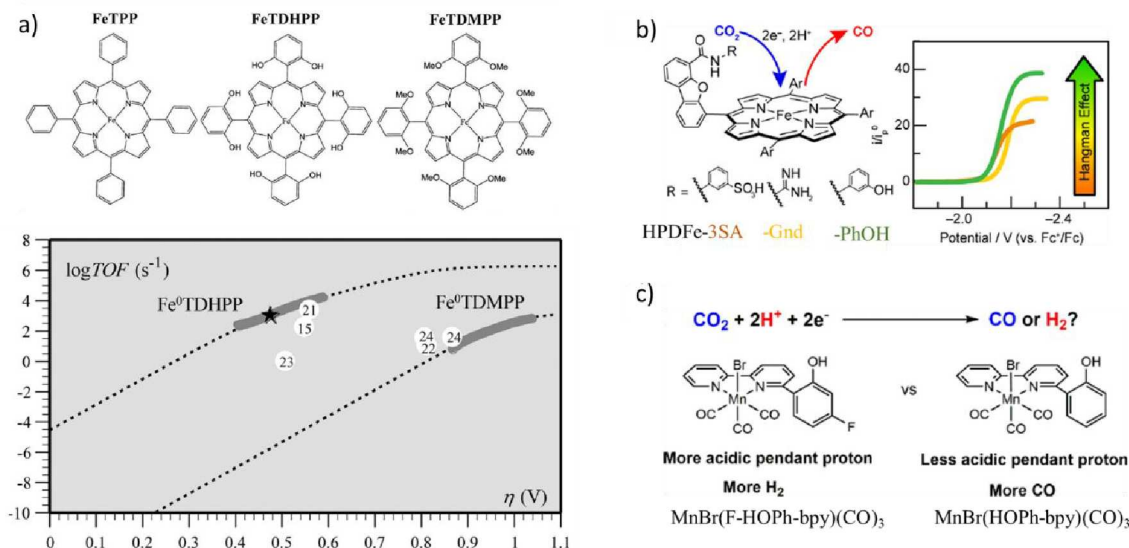


**Figure 9.** a) Correlation between turnover frequency  $\log TOF$  and overpotential  $\eta$  for FeTPP, FeTDHPP, FeTDMPP and a series of cited catalysts for comparison listed in the table. Thick gray segments represent TOF values calculated from Foot-of-the-wave analysis of catalytic CVs of FeTDHPP and FeTDMPP in DMF with 2.0 M H<sub>2</sub>O. Dashed lines show the Tafel plots for FeTDHPP and FeTDMPP in DMF with 2.0 M H<sub>2</sub>O respectively. The star represents the (TOF,  $\eta$ ) data point of FeTDHPP and circled numbers represent (TOF,  $\eta$ ) data points of cited catalysts from preparative-scale experiments. Adapted with permission from *Science* **2012**, *338*, 90-94.<sup>65</sup> Copyright © 2012, American Association for the Advancement of Science; b) The structures of HPDFe-3SA, HPDFe-Gnd and HPDFe-PhOH and their corresponding catalytic current for the CO<sub>2</sub>RR, adapted with permission from *Organometallics* **2019**, *38*, 6, 1219–1223.<sup>72</sup> Copyright 2019, American Chemical Society; c) Schematic comparison of catalytic performance between MnBr(F-HOPh-bpy)(CO)<sub>3</sub> with more acidic pendant proton relays and MnBr(2,2'-bipyridine)(CO)<sub>3</sub> with less acidic pendant proton relays, adapted with permission from *Organometallics* **2020**, *39*, 13, 2425–2437.<sup>87</sup> Copyright 2020, American Chemical Society.

In another example, MnBr(6-(2-hydroxyphenyl)-2,2'-bipyridine)(CO)<sub>3</sub> ((MnBr(HOPh-bpy)(CO)<sub>3</sub>) with an acidic phenolic group in close proximity to the Mn center breaks typical molecular scaling relationships by operating at lower effective overpotential and seven times higher activity for the CO<sub>2</sub>RR compared to MnBr(2,2'-bipyridine)(CO)<sub>3</sub> ((MnBr(bpy)(CO)<sub>3</sub>).<sup>88</sup> The enhanced catalytic ability of MnBr(HOPh-bpy)(CO)<sub>3</sub> is attributed to the increased acidic phenolic proton concentration proximate to the Mn center, which is proposed to facilitate proton-assisted C-O bond cleavage of reduced CO<sub>2</sub> intermediates.<sup>88</sup> However,

increasing the acidity of proton donors in the secondary coordination sphere does not always lead to more efficient catalysts for the CO<sub>2</sub>RR. (MnBr(F-HOPh-bpy))(CO)<sub>3</sub> with more acidic fluoro-phenolic groups in the structure (**Figure 9c**) exhibits decreased partial catalytic current and decreased reaction selectivity for the CO<sub>2</sub>RR compared to (MnBr(HOPh-bpy))(CO)<sub>3</sub>.<sup>87</sup> Spectro-electrochemical measurements and DFT studies suggest that Mn(I) hydride is generated more easily for MnBr(F-HOPh-bpy)(CO)<sub>3</sub> with more acidic phenolic proton proximate to the Mn center compared to (MnBr(HOPh-bpy))(CO)<sub>3</sub>, leading to increased competitive H<sub>2</sub> production at the expense of CO<sub>2</sub> reduction.<sup>87</sup>

#### 4.2.b. Enhancing H-bonding Interactions between Proton Relays and Reduced CO<sub>2</sub> adducts in the Secondary Coordination Sphere.

Less acidic proton relays such as methoxy,<sup>89, 90</sup> amine,<sup>67, 68, 70, 71, 91, 92</sup> amide,<sup>69, 71</sup> imidazolium,<sup>66, 93</sup> urea,<sup>71</sup> and thiourea<sup>94</sup> groups have been incorporated into the secondary coordination sphere of molecular catalyst to tune catalytic activity for the CO<sub>2</sub>RR. Instead of protonating the CO<sub>2</sub>-adduct directly, these less acidic moieties are thought to stabilize reduced CO<sub>2</sub> intermediates by establishing an H-bonding network involving the proton relay and the solution proton source. This H-bonding network facilitates proton transfer from the solution proton sources to the CO<sub>2</sub> adduct, and thus facilitates CO<sub>2</sub> activation and C-O bond cleavage.<sup>67-71, 89-92, 94, 95</sup>

For example, the Mn bipyridyl tricarbonyl complex *fac*-Mn'([(MeO)<sub>2</sub>Ph]<sub>2</sub>bpy)(CO)<sub>3</sub>(CH<sub>3</sub>CN)(OTf) contains four pendant methoxy groups in the ligand 6,6'-bis(2,6-dimethoxyphenyl)-2,2'-bipyridine ([[(MeO)<sub>2</sub>Ph]<sub>2</sub>bpy]) (**Figure 10a**) and operates with good catalytic activity for the CO<sub>2</sub>RR with high product selectivity for CO. This catalyst is proposed to operate through a protonation-first pathway that occurs at least 0.55 V lower overpotential compared to the thermodynamically demanding reduction-first pathway (**Figure 10a**).<sup>89</sup> Spectroelectrochemical studies and DFT analysis suggest that H-bonding interactions between the pendant -OMe groups, the Brønsted acid in solution, and the Mn-CO<sub>2</sub> adduct dramatically decrease the energy barrier for protonation and C-O bond cleavage of the Mn-carboxylic intermediate, leading to the protonation-first pathway at the lower overpotential.<sup>89</sup>

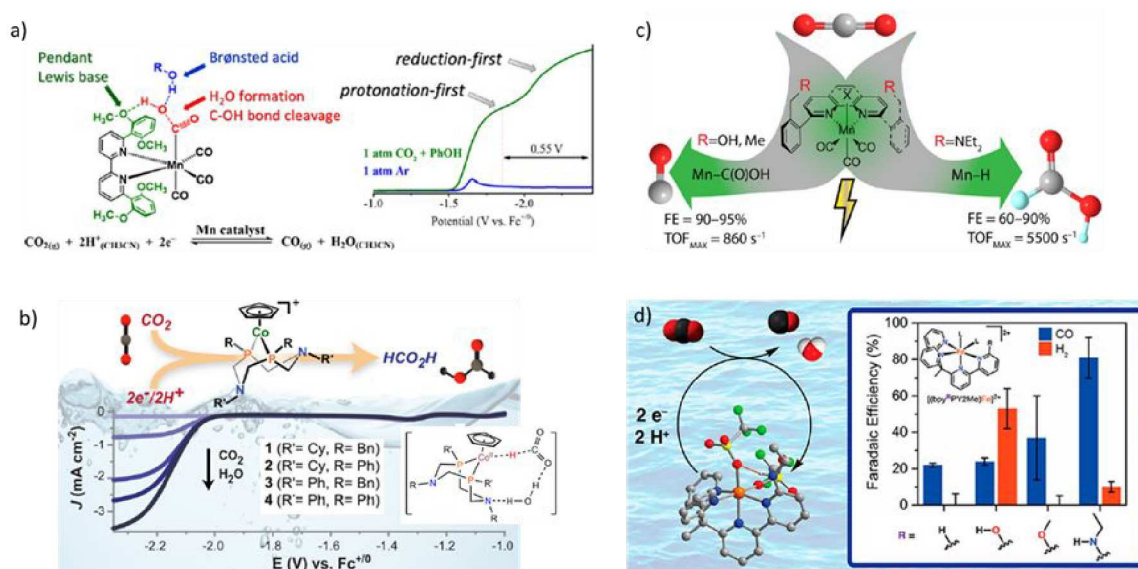


**Figure 10.** a) *fac*-Mn<sup>I</sup>([(MeO)<sub>2</sub>Ph]<sub>2</sub>bpy)(CO)<sub>3</sub>(CH<sub>3</sub>CN)(OTf) with four pendant methoxy groups establishes an allosteric H-bonding network among pendant -OMe groups, solution Brønsted acids, and the Mn-CO<sub>2</sub> adduct. This H-bonding network results in a *protonation-first* mechanistic pathway of reducing CO<sub>2</sub> at lower overpotentials. Adapted with permission from *J. Am. Chem. Soc.* **2017**, 139, 7, 2604–2618.<sup>89</sup> Copyright 2017 American Chemical Society; b) a series of [CpCo(P<sup>R</sup><sub>2</sub>N<sup>R'</sup><sub>2</sub>)I]<sup>+</sup> complexes containing two pendant amine residues in P<sup>R</sup><sub>2</sub>N<sup>R'</sup><sub>2</sub> ligand show increased activity for selective CO<sub>2</sub> reduction to HCOOH by facilitating the hydride transfer from the Co site to the CO<sub>2</sub> molecule through H-bonding interactions with the proton source H<sub>2</sub>O. Adapted with permission from *J. Am. Chem. Soc.* **2017**, 139, 10, 3685–3696.<sup>68</sup> Copyright 2017 American Chemical Society; c) Ligand-controlled product selectivity for the CO<sub>2</sub>RR by a series of Mn complexes with modified bipyridine or phenanthroline ligands with different pendant proton relay groups in the secondary coordination sphere. Adapted with permission from *J. Am. Chem. Soc.* **2020**, 142, 9, 4265–4275.<sup>91</sup> Copyright 2020, American Chemical Society; d) A family of polypyridyl-iron [(bpy<sup>R</sup>PY2Me)Fe<sup>II</sup>] complexes show varying selection for CO<sub>2</sub>RR or HER with different pendant proton relay groups with varying acidities (-H, -OH, -OMe AND -NH<sub>2</sub>). Adapted with permission from *Inorg. Chem.* **2020**, 59, 7, 5206–5217.<sup>95</sup> Copyright 2020, American Chemical Society.

In another example, a series of [CpCo(P<sup>R</sup><sub>2</sub>N<sup>R'</sup><sub>2</sub>)I]<sup>+</sup> complexes containing two pendant amine residues incorporated into the P<sup>R</sup><sub>2</sub>N<sup>R'</sup><sub>2</sub> ligand has been used to modulate the catalyst's activity and product selectivity for the CO<sub>2</sub>RR (Figure 10b).<sup>68</sup> In particular, complex 4 in Figure 10b has the most electron-donating phosphine ligand and the most basic amine moieties, and operates with the highest CO<sub>2</sub>RR

activity for the selective reduction of CO<sub>2</sub> to HCOOH. This complex is one of the most active molecular catalysts reported for selective CO<sub>2</sub> reduction to HCOOH with a TOF > 10<sup>3</sup> s<sup>-1</sup>. Mechanistic studies and DFT calculations suggest that the pendant amine groups in the secondary coordination sphere of these [CpCo(PR<sub>2</sub>N<sup>R'</sup><sub>2</sub>)]<sup>+</sup> complexes play a crucial role in stabilizing CO<sub>2</sub>-adduct intermediates through H-bonding interactions with the proton source H<sub>2</sub>O, and facilitate hydride transfer from the Co site to the CO<sub>2</sub> molecule to generate the final HCOOH product.<sup>68</sup>

Introducing proton relays within the secondary coordination sphere of molecular catalysts can not only enhance the catalytic activity for the CO<sub>2</sub>RR, but also modulate the selectivity for different products. For example, ligand-controlled product selectivity for the CO<sub>2</sub>RR was observed for a series of Mn complexes with modified bipyridine and phenanthroline ligands (**Figure 10c**).<sup>91, 92</sup> Mn complexes incorporating -OH and -Me groups in the secondary coordination sphere reduce CO<sub>2</sub> to CO with TOF<sub>max</sub> ~ 860 s<sup>-1</sup>, whereas Mn complexes incorporating tertiary amines (-NEt<sub>2</sub>) positioned proximate to the metal center reduce CO<sub>2</sub> to HCOOH with greater TOF<sub>max</sub> ~ 5500 s<sup>-1</sup> at even 300 mV lower effective overpotential than the -OH and -Me analogs.<sup>91</sup> This increased activity and altered selectivity of the CO<sub>2</sub> reduction to HCOOH was attributed to the *in situ* protonated amine groups in the secondary coordination sphere aiding in the formation of Mn-hydride intermediates in the HCOOH production pathway.<sup>91, 92</sup> This conclusion was supported by infrared spectroelectrochemistry and DFT analysis of these complexes.<sup>91, 92</sup> A similar phenomenon was also observed for a family of polypyridyl-iron [(bpy<sup>R</sup>PY2Me)Fe<sup>II</sup>] complexes which achieve increasing selectivity for CO<sub>2</sub>RR over competitive HER by modulating the acidity of groups in the secondary coordination sphere—incorporating strongly acidic groups such as -OH promote competitive HER, while incorporating weakly-acidic groups such as NH<sub>2</sub> promote the CO<sub>2</sub>RR (**Figure 10d**).<sup>95</sup>

To ascertain the correlation between the number of proton relays in the secondary coordination sphere and a molecular catalyst's CO<sub>2</sub>RR activity, researchers studied a series of Co aminopyridine macrocycle complexes with varying number of (-NH) and tertiary (-NMe) amines in the ligand scaffold (**Figure 11a**).<sup>70</sup> Electrochemical and kinetic studies of these Co complexes revealed that higher catalytic rate was obtained by increasing the number of -NH groups in the secondary coordination sphere (**Figure 11b**). This

experimental result is consistent with DFT results that show that increasing the number of –NH groups in the secondary coordination sphere leads to more negative CO<sub>2</sub> binding free energy (**Figure 11c**). The pendant NH groups facilitate the proton transfer from external proton sources to the CO<sub>2</sub>-adduct through a H-bonding network, resulting in the more favorable calculated CO<sub>2</sub> binding free energies and the experimentally-observed increase in activity with increasing number of –NH groups in the secondary coordination sphere.<sup>67</sup>

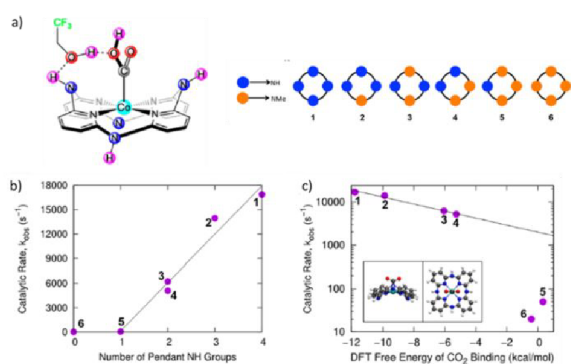


**Figure 11.** a) The structure of Co aminopyridine macrocycle complexes with varying number of NH and NMe groups in the ligand scaffold; b) the correlation between catalytic rate and number of pendant NH group in the secondary coordination sphere; c) the correlation between catalytic rate and DFT free energy of CO<sub>2</sub> binding. Adapted with permission from *ACS Cent. Sci.* 2018, 4, 3, 397–404<sup>70</sup>, <https://pubs.acs.org/doi/abs/10.1021/acscentsci.7b00607>. Copyright 2018 American Chemical Society, further permissions related to the material excerpted should be directed to the ACS.

In another example exploring how the number of proton relays in the secondary coordination sphere influence catalytic activity for the CO<sub>2</sub>RR, FeTPP complexes were decorated with H-bonding pillars incorporating either H-bonding urea groups in FeTPP-Ur or amido groups in FeTPP-Am (**Figure 12a**).<sup>71</sup> Both FeTPP-Ur and FeTPP-Am show significantly enhanced activity for the CO<sub>2</sub>RR compared to the parent FeTPP complex, and break typical molecular scaling relationships (**Figure 12b**).<sup>71</sup> However, FeTPP-Ur achieves the same TOF<sub>max</sub> compared to FeTPP-Am at much lower effective overpotential. The increased activity of FeTPP-Ur is attributed to the increased H-bonding capability of the multipoint H-bonding pillars in the FeTPP-Ur compared to that of the single-point H-bonding pillars in FeTPP-Am (**Figure 12a**).<sup>71</sup>

Proper positioning of pendant proton relays is also important in modulating catalytic activity of molecular catalysts for the CO<sub>2</sub>RR. For example, four FeTPP complex derivatives bearing proximal and distal pendant amide groups in the TPP scaffold (**Figure 12c**) all departed from typical molecular scaling relationships for FeTPP-based complexes (**Figure 12d**).<sup>69</sup> However, the performance of the amide-modified catalysts changes based on the positioning of the amide groups in the ligand structure. Adjusting the position of amide groups in these Fe complexes does not affect the catalysts' effective overpotentials for the CO<sub>2</sub>RR, but the Fe-*ortho*-1-amide and Fe-*ortho*-2-amide complexes operate with higher turnover frequency than their respective *para*-amide analogs: Fe-*para*-1-amide and Fe-*para*-2-amide. This increased activity for the *ortho*-amide complexes compared to the *para*-amide complexes is attributed to more effective through-space H-bonding interactions between the CO<sub>2</sub>-adduct and the *ortho*-amide moieties due to their closer proximity to the CO<sub>2</sub>-binding site (**Figure 12c**).<sup>69</sup> Moreover, Fe-*ortho*-2-amide shows more than two orders of magnitude higher TOF compared to Fe-*ortho*-1-amide (**Figure 12d**) due to the closer proximity of the H-bonding amide moiety to the active site for Fe-*ortho*-2-amide (**Figure 12c**).<sup>69</sup> This result further demonstrates that tuning the position of proton relays in the secondary coordination sphere is an effective approach to design more-efficient molecular catalysts that break molecular scaling relationships.

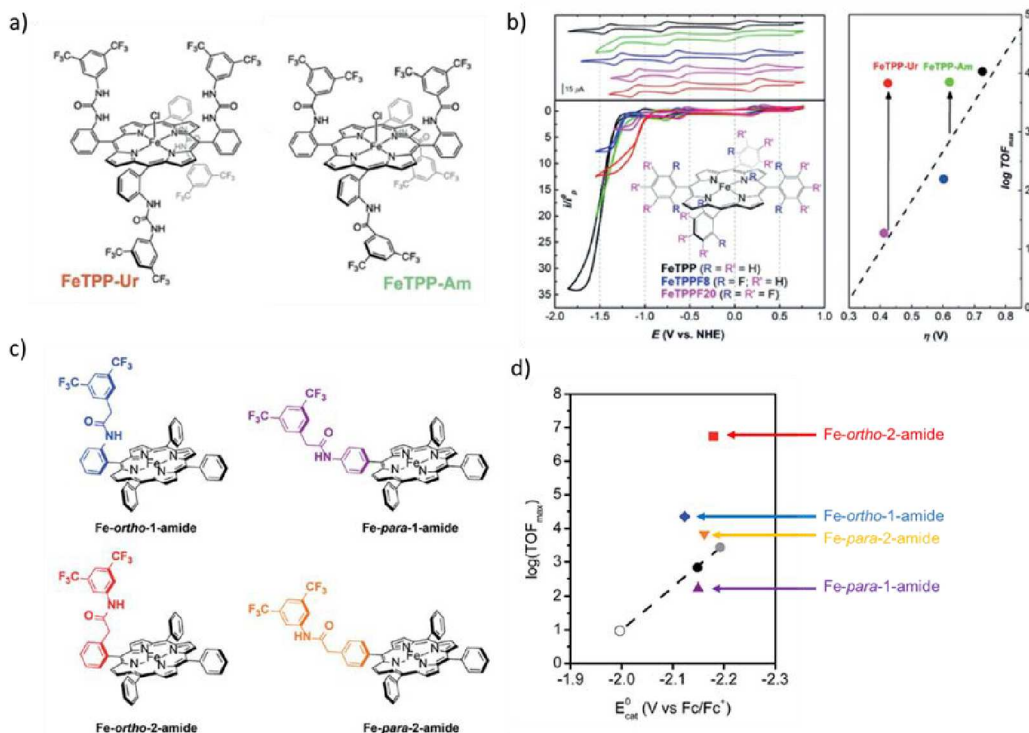


**Figure 12.** a) The structures of FeTPP-Ur and FeTPP-Am; b) Left: CVs of FeTPP-Ur (red) and FeTPP-Am (green) compared to other FeTPP derivatives in DMF solution with 0.1 M Bu<sub>4</sub>NPF<sub>6</sub> under argon (top left) and under CO<sub>2</sub> with 5.5 M water as proton source (bottom left); Right: correlations between logTOF<sub>max</sub> and catalytic overpotential  $\eta$  for different FeTPP derivatives. The dashed line represents the scaling relationship of FeTPP derivatives without secondary coordination sphere effects; a) and b) adapted with permission from *Angew. Chem. Int. Ed.* **2019**, 58, 4504–4509.<sup>71</sup> 2019 Wiley-VCH Verlag GmbH & Co. KGaA, Weinheim. c) The structures of positional isomers of amide-functionalized FeTPP complexes; d) Correlations between log(TOF<sub>max</sub>) and the redox potentials of complexes for Fe-ortho-1-amide, Fe-ortho-2-amide, Fe-para-1-amide and Fe-para-2-amide. The dashed line represents the scaling relationship of FeTPP derivatives without secondary coordination sphere effects; c) and d) adapted with permission from *Chem. Sci.*, **2018**, 9, 2952,<sup>69</sup> - Published by The Royal Society of Chemistry.

#### 4.3. Designing Binuclear Metal Complexes that Synergistically Coordinate and Activate CO<sub>2</sub>.

In the natural enzyme Ni,Fe-CODH, the active binuclear Ni-Fe cluster is an important structural feature that leads to the enzymes high activity for reversible CO<sub>2</sub> reduction to CO.<sup>86</sup> In particular, the Ni center is proposed to coordinate the C atom of CO<sub>2</sub> at an active reducing site, while the Fe center interacts with one O atom of CO<sub>2</sub> as a Lewis acidic site and assists in the protonation and C-O bond cleavage of the

intermediate.<sup>86</sup> The structural feature of Ni-Fe cluster offers a promising strategy for designing binuclear molecular catalysts with appropriately positioned metal sites that are able to synergistically coordinate and activate CO<sub>2</sub>. However, there are relative few recent examples of synthetic bimetallic metal complexes reported for the CO<sub>2</sub>RR that operate via a mechanism involving synergistic CO<sub>2</sub> binding,<sup>96-99</sup> possibly due to the difficulty in synthesizing and characterizing such systems.

One example is a binuclear cobalt cryptate complex (CoCoL<sup>1</sup>, **Figure 13a**) reported to photocatalytically reduce CO<sub>2</sub> to CO with significantly higher turnover number (TON = 16896) and improved selectivity (Faradaic efficiency, FE = 98%) compared to its mononuclear Co analog (CoL<sup>2</sup>, TON = 1600, FE = 85%).<sup>96</sup> In a photocatalytic system, there is no applied electrochemical potential. Instead, the reducing ability of the photosensitizer is the driving force behind activating the molecular complex for the catalytic reaction. Thus, the equivalent scaling relationships in photocatalytic systems is a correlation between increased reducing ability of the photosensitizer and increased activity for the photocatalytic CO<sub>2</sub>RR. In the case of the CoCoL<sup>1</sup> system, the observed increase in activity using the same photosensitizer compared to the mononuclear analog CoL<sup>2</sup> suggests a deviation from this normal scaling relationship. This increased activity of CoCoL<sup>1</sup> is attributed to the synergistic coordination and activation of CO<sub>2</sub> between the two Co sites—one Co site is thought to bind and reduce CO<sub>2</sub> while the other Co site serves as a Lewis acid to stabilize reduced CO<sub>2</sub> adducts and facilitate C-O bond cleavage.<sup>96</sup> The postulated role of these two sites was further supported by kinetic studies showing a first-order dependence of rate on CoCoL<sup>1</sup> concentration consistent with only one CO<sub>2</sub> coordinating per complex, and DFT calculations suggesting the formation of an intermediate with one CO<sub>2</sub> molecular trapped between the two intramolecular Co sites in the CoCoL<sup>1</sup> structure.<sup>96</sup>

Based on the results with CoCoL<sup>1</sup>, researchers have also explored the heterobimetallic CoZnL<sup>1</sup> complex for the CO<sub>2</sub>RR (**Figure 13a**). In CoZnL<sup>1</sup>, the Co site acts as the active site for CO<sub>2</sub> coordination and reduction, and Zn replaces the other Co as a more Lewis acidic site to facilitate C-O bond cleavage.<sup>97</sup> The CoZnL<sup>1</sup> complexes photocatalytically reduces CO<sub>2</sub> to CO with four times higher activity compared to CoCoL<sup>1</sup>, and 45 times higher activity compared to the monometallic CoL<sup>2</sup> parent complex.<sup>97</sup> The higher activity for

CoZnL<sup>1</sup> is attributed to the increased binding affinity of Zn to the O atom in CO<sub>2</sub>, strengthening the synergistic cooperation between the Zn and Co sites in CoZnL<sup>1</sup> compared to that of the Co sites in CoCoL<sup>1</sup>. Control experiments in which Zn<sup>2+</sup> was added into solutions containing CoL<sup>2</sup> and CoCoL<sup>1</sup> complexes showed no enhancement in photocatalytic CO<sub>2</sub> reduction activity, confirming that optimal positioning of the Lewis acidic site is crucial to enable synergistic bimetallic CO<sub>2</sub> activation.<sup>97</sup>

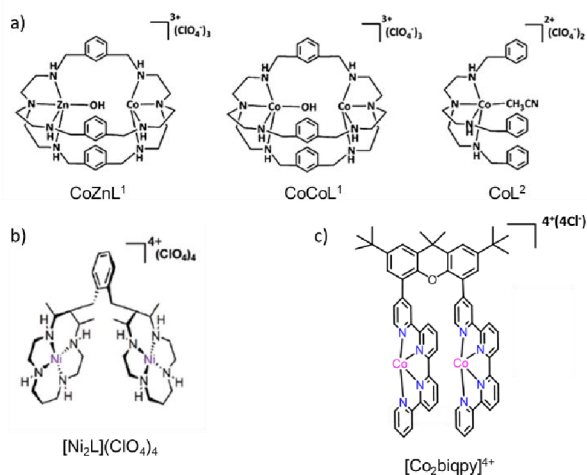


**Figure 13.** a) The structures of CoZnL<sup>1</sup>, CoCoL<sup>1</sup> and CoL<sup>2</sup> (L<sup>1</sup>, L<sup>2</sup> = cryptate ligands), adapted with permission from *Angew. Chem. Int. Ed.* **2018**, 57, 16480–16485.<sup>97</sup> 2018 Wiley-VCH Verlag GmbH & Co. KGaA, Weinheim; b) The structure of [Ni<sub>2</sub>L](ClO<sub>4</sub>)<sub>4</sub> (L = 1,2-bis((5,7-dimethyl-1,4,8,11-tetraazacyclotetradecan-6-yl)methyl)benzene), adapted with permission from *Green Chem.*, **2018**, 20, 798-803.<sup>98</sup> with permission from The Royal Society of Chemistry; c) The structure of [Co<sub>2</sub>biqpy]<sup>4+</sup> (biqpy = 4,4''''-(2,7-di-*tert*-butyl-9,9-dimethyl-9*H*-xanthene-4,5-diyl)).<sup>99</sup>

Other examples of binuclear complexes that reduce CO<sub>2</sub> via cooperative CO<sub>2</sub> binding and activation mechanism include the binuclear Ni complex [Ni<sub>2</sub>L](ClO<sub>4</sub>)<sub>4</sub> shown in **Figure 13b**,<sup>98</sup> and the binuclear Co complex [Co<sub>2</sub>biqpy]<sup>4+</sup> shown in **Figure 13c**.<sup>99</sup> Both of these complexes operate with dramatically enhanced electrocatalytic activity for the CO<sub>2</sub>RR compared to their mononuclear analogues. Although there are comparatively few studies reporting binuclear complexes that cooperatively coordinate and reduce CO<sub>2</sub>, the aforementioned studies provide a promising strategy to optimize catalytic activity and break the molecular scaling relationships through synergistic CO<sub>2</sub> coordination and activation.

## 5. Combining Kinetic and Thermodynamic Approaches to Break Molecular Scaling Relationships

The strategies highlighted in the previous section for breaking molecular scaling relationships have focused primarily on kinetic approaches: stabilizing CO<sub>2</sub>-adduct intermediates to decrease the activation energy  $E_A$  through intramolecular electrostatics, H-bonding effects, facilitated proton transport, or binuclear synergistic coordination modes (**Figure 14a**). These kinetic approaches typically result in catalysts with increased TOF for the CO<sub>2</sub>RR, but that operate with similar effective overpotentials compared to their parent systems. In contrast, there are very few examples of breaking molecular scaling relationships using a thermodynamic approach that modulates the redox potential of the metal center (**Figure 14a**). This is because in most catalysts, a metal-based redox event immediately precedes catalytic onset. Thus, the catalyst redox potential  $E_{cat/2}$  is correlated to the nucleophilicity of the metal center. Positive shift in  $E_{cat/2}$  leads to decreased nucleophilicity, which in turn results in lower binding affinity to the substrate.<sup>34, 44, 48, 52,</sup>

55

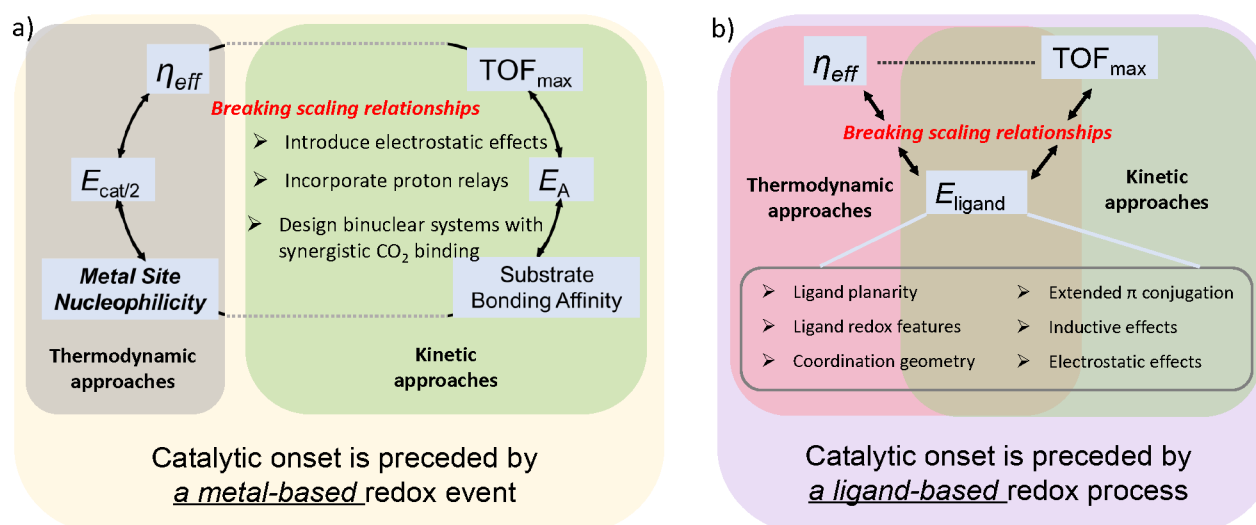


**Figure 14.** a) The reported strategies of breaking the scaling relationship for the molecular catalysts where the catalytic onset is preceded by the metal-based redox event; b) The strategies of the McCrory Lab for breaking the scaling relationship by using the molecular catalysts with redox active ligands, where the catalytic onset is preceded by the ligand-based redox process.

In our group, we have focused on designing molecular catalysts with redox active ligands in which catalytic onset is preceded by the formation of a ligand radical in a *ligand-based redox process* rather than

a metal-based redox event. In this scenario,  $E_{\text{cat}/2}$  and the metal site nucleophilicity are no longer necessarily correlated, and both kinetic and thermodynamic approaches can be implemented to break molecular scaling relationships (**Figure 14b**). In this section, we will introduce recent progress in our lab designing more-efficient molecular catalysts with redox-active ligands that break *molecular scaling relationships* for the CO<sub>2</sub>RR.

### 5.1. Modulating the Electronic Structure of Complexes with Redox-Active Ligands through Substituent Effects.

The pyridyldimine (PDI) ligand is a well-known redox-active ligand that can be reduced by one electron to a ligand radical stabilized by its electron-conjugated structure (**Figure 15a**).<sup>100, 101</sup> Co complexes with PDI ligands, in particular [Co(PDI)], have been reported as moderate catalysts for the CO<sub>2</sub>RR in acetonitrile solutions using H<sub>2</sub>O as the proton source, forming CO with ~45% Faradaic efficiency.<sup>102</sup> Spectroscopic and DFT studies of the CO<sub>2</sub>RR by [Co(PDI)] revealed that the redox-process immediately preceding catalytic onset is a ligand-based reduction: a reduction of [Co<sup>I</sup>(PDI)]<sup>+</sup> complex to [Co<sup>I</sup>(PDI<sup>•-</sup>)]<sup>0</sup>, with the ligand radical located primarily on the imine carbons.<sup>103</sup> The fact that a ligand-based reduction precedes catalytic onset for CO<sub>2</sub>RR makes [Co(PDI)] a suitable model system for exploring our strategy of breaking molecular scaling relationships by simultaneously implementing both kinetic and thermodynamic approaches.

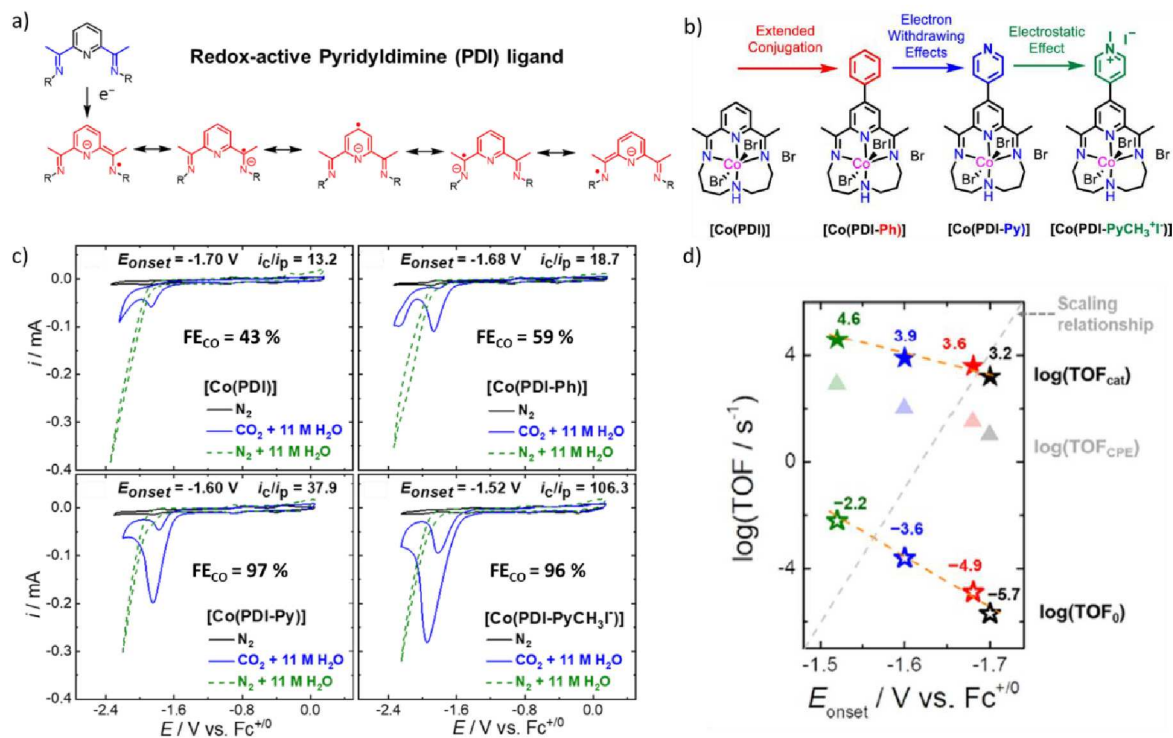


**Figure 15.** a) Schematic representation of the one-electron reduction of the redox-active PDI ligand forming a ligand radical; b) Sequentially introducing three synergistic substituent effects into the PDI-ligand scaffold of the [Co(PDI)] complex results in the [Co(PDI-Ph)], [Co(PDI-Py)] and [Co(PDI-PyCH<sub>3</sub><sup>+</sup>)] complexes; c) Catalytic CVs of this series of Co-PDI based catalysts for the CO<sub>2</sub>RR using 11.0 M H<sub>2</sub>O as a proton source show a corresponding positive shift in the catalytic onset potential ( $E_{\text{onset}}$ ) and an increase in the catalyst's activity ( $i_c/i_p$ ) as each substituent effect is sequentially introduced into the PDI ligand structure; d) An *inverse scaling relationship* between the catalytic onset potential ( $E_{\text{onset}}$ ) and catalytic activity (TOFs) is observed among this series of Co-PDI based catalysts. b-d) are adapted with permission from *J. Am. Chem. Soc.* **2021**, 143, 10, 3764–3778.<sup>104</sup> Copyright 2021 American Chemical Society

In our recent study with the [Co(PDI)]-based systems, we incorporated electronic substituents that both shift the potential of the PDI ligand more positive by stabilizing ligand radicals (a thermodynamic approach), and also increased catalytic turnover by facilitating the storage of charge equivalents in the ligand, which in turn facilitate the formation and stabilization of the reduced CO<sub>2</sub> intermediate (a kinetic approach).<sup>93</sup> Based on this overall strategy, we sequentially introduced three synergistic substituent effects into the PDI-ligand scaffold (**Figure 15b**): introducing a phenyl group to extend ligand conjugation ([Co(PDI-Ph)]), adding a pyridyl group to increase the

ligand's electron withdrawing ability ([Co(PDI-Py)]), and incorporating a cationic *N*-methylpyridinium group to introduce intramolecular electrostatic effects ([Co(PDI-PyCH<sub>3</sub><sup>+</sup>I<sup>-</sup>)].<sup>104</sup> As each substituent effect is sequentially introduced into the system, there is a corresponding positive shift in the catalytic onset potential ( $E_{\text{onset}}$ ) and an increase in the catalyst's activity ( $i_c/i_p$ ) for the CO<sub>2</sub>RR using 11.0 M H<sub>2</sub>O as a proton source (**Figure 15c**). In addition, the Faradaic efficiency for CO<sub>2</sub> reduction to CO (FE<sub>CO</sub>) measured from controlled potential electrolysis experiments increased with sequential addition of the electronic substituents: from ~45% for the parent [Co(PDI)] complex to ~59% for [Co(PDI-Ph)], to >95% for [Co(PDI-Py)] and [Co(PDI-PyCH<sub>3</sub><sup>+</sup>I<sup>-</sup>)].<sup>104</sup> Turnover frequencies of this series of [Co(PDI-R)] catalysts estimated from kinetic voltammetric studies, the maximum TOF<sub>cat</sub> and intrinsic activity parameter TOF<sub>0</sub>, both show increased activity with increasing  $E_{\text{onset}}$ —an *inverse scaling relationship* (**Figure 15d**). The most active catalyst of the series, [Co(PDI-PyCH<sub>3</sub><sup>+</sup>I<sup>-</sup>)], incorporates all three synergistic substituent effects into a single catalyst structure and is among the most active molecular catalysts reported for the CO<sub>2</sub>RR. This work highlights the promise of our strategy to break molecular scaling relationships by modulating the electronic structure of catalysts with redox-active ligands where ligand reduction immediately precedes catalytic onset.

## 5.2. Modulating the Coordination Geometry of Molecular Catalysts by Changing the Flexibility and Planarity of Redox-Active Ligands.

An alternative ligand structure explored by our lab links redox-active pyridylmonimine moieties (**Figure 16a**) with aliphatic linkers to form bispyridylmonoimine ligands (**Figure 16b**). Co complexes with this ligand are denoted interchangeably [Co(L-L)Br<sub>2</sub>]Br and [Co(L-L)], and show high activity for the reduction of CO<sub>2</sub> to CO with Faradaic Efficiency > 80% for CO production in acetonitrile solutions with either 11 M H<sub>2</sub>O or 5.5 M trifluoroethanol as the proton source (**Figure 16c**).<sup>105</sup> Similar to the [Co(PDI)]-based complexes, reduction of [Co<sup>I</sup>(L-L)] to the [Co<sup>I</sup>(L-L<sup>•-</sup>)] with a ligand radical is thought to immediately precede the onset of the CO<sub>2</sub>RR.<sup>105</sup>

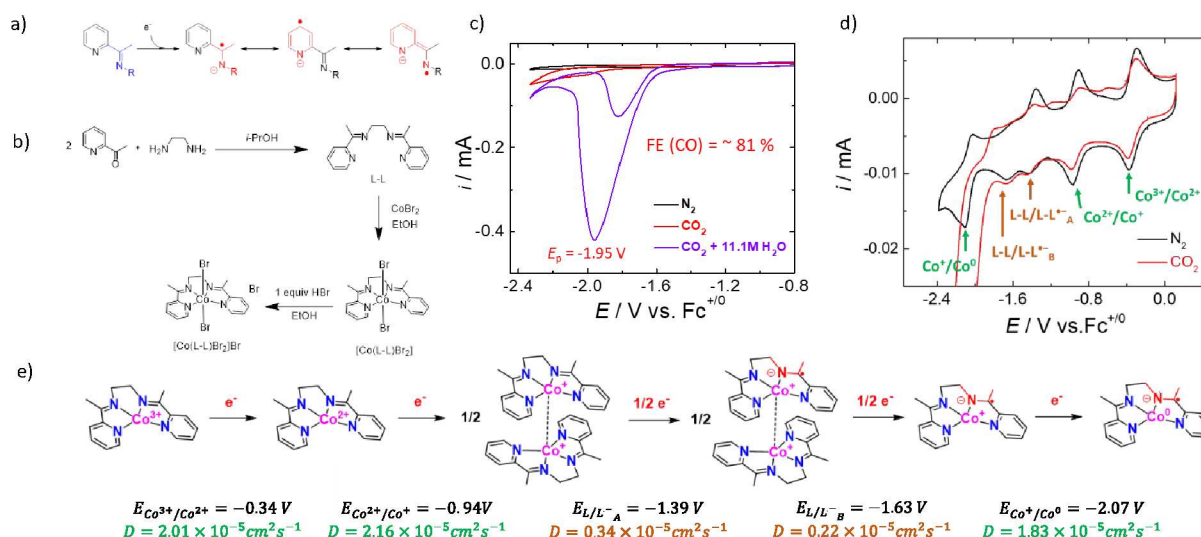


**Figure 16.** a) Schematic representation of the one-electron reduction of a redox-active pyridylmonoimine moiety forming a ligand-radical; b) The synthesis of the cobalt complex [Co(L-L)] with the bis(pyridylmonoimine) ligand containing two pyridylmonoimine connected by an ethylene bridge; c) Catalytic CVs of the  $\text{CO}_2\text{RR}$  by [Co(L-L)] in MeCN with 11.0 M  $\text{H}_2\text{O}$  as the proton source. The catalyst has high activity and Faradaic efficiency for CO production; d) A zoom-in of the onset region for the  $\text{CO}_2\text{RR}$  by the [Co(L-L)] complex shows the delayed catalytic onset for the  $\text{CO}_2\text{RR}$  due to the reductive dimerization process; e) The proposed structures of [Co(L-L)] species at each redox potential for the reductive dimerization pathway with corresponded diffusion coefficients. a), b) and e) are adapted with permission from *ACS Catal.* **2020**, 10, 9, 4942–4959.<sup>106</sup> Copyright 2020, American Chemical Society; c) is adapted with permission from *Chem. Commun.*, **2018**, 54, 1579.<sup>105</sup> The Royal Society of Chemistry.

However, additional electroanalytical studies suggested [Co(L-L)] undergoes reductive dimerization upon reduction to the  $\text{Co}^{\text{I}}$  state. This was evidenced by two small redox features subsequent to the  $\text{Co}^{\text{II/I}}$  couple that are assigned to the stepwise reduction of each ligand in the  $[\text{Co}^{\text{I}}(\text{L-L})]_2$  dimer (**Figure 16d**).<sup>106</sup> Scan-rate dependence studies and rotating-disk voltammetry studies of these ligand-based features also suggested a decrease in the diffusion coefficient of the complex upon reduction to  $[\text{Co}^{\text{I}}(\text{L-L})]_2$ , consistent with formation of a  $[\text{Co}^{\text{I}}(\text{L-L})]_2$  dimer species (**Figure 16e**).<sup>106</sup> Upon the second ligand reduction, the dimer dissociates resulting in the catalytically-active  $[\text{Co}^{\text{I}}(\text{L-L}^{\cdot-})]$  species.<sup>106</sup> Because the catalytic onset occurs only after reduction of the second L-L feature at  $E_{\text{L-L}^{\cdot-}_B}$  and subsequent dimer dissociation, the  $E_{\text{onset}}$  for the  $\text{CO}_2\text{RR}$  is more negative than we would expect compared to a hypothetical monomer  $\text{Co}(\text{L-L})$  species in

which catalytic onset would occur immediately following ligand reduction at the more positive potential  $E_{L-L, A}$ .

To prevent this dimerization, we altered the flexibility of the aliphatic bridge in the ligand scaffold. We hypothesized that increasing ligand flexibility would distort the square-planar coordination environment of the  $\text{CoN}_4$  active site. This distortion would decrease the planarity of the complex and inhibit dimerization, thus shifting  $E_{\text{onset}}$  more positive. In accordance with our hypothesis, we synthesized a series of  $[\text{Co}(\text{L-R-L})]$  with more flexible ligand scaffolds (**Figure 17a**).<sup>106</sup> Non-catalytic CVs of the  $[\text{Co}(\text{L-R-L})]$  complexes exhibited only one reversible ligand-based feature, instead of two smaller redox features in  $[\text{Co}(\text{L-L})]$ . In addition, scan-rate dependence and rotating-disk voltammetry experiments of the ligand-based features also suggested there was no appreciable change in the diffusion coefficient for the complex upon reduction to  $[\text{Co}^{\text{I}}(\text{L-L})]$ .<sup>106</sup> Interestingly, the  $\text{Co}^{\text{II/I}}$  redox potential was shifted negative in the  $[\text{Co}(\text{L-R-L})]$  complexes compared to  $[\text{Co}(\text{L-L})]$ , suggesting that the  $\text{Co}^{\text{I}}$  site is more nucleophilic in the  $[\text{Co}(\text{L-R-L})]$  complexes. The  $[\text{Co}(\text{L-R-L})]$  complexes operated with more positive  $E_{\text{onset}}$  and slightly increased activity for the  $\text{CO}_2\text{RR}$  compared to  $[\text{Co}(\text{L-L})]$  in acetonitrile with trace water ( $\sim 0.04$  M) as the proton source (**Figure 17b**),<sup>106</sup> breaking molecular scaling relationships. The shift in  $E_{\text{onset}}$  was attributed to the inhibition of dimerization in the  $[\text{Co}(\text{L-R-L})]$  complexes as hypothesized, and the increase in activity was attributed to the increased nucleophilicity of the  $\text{Co}^{\text{I}}$  site facilitating  $\text{CO}_2$  binding and activation.

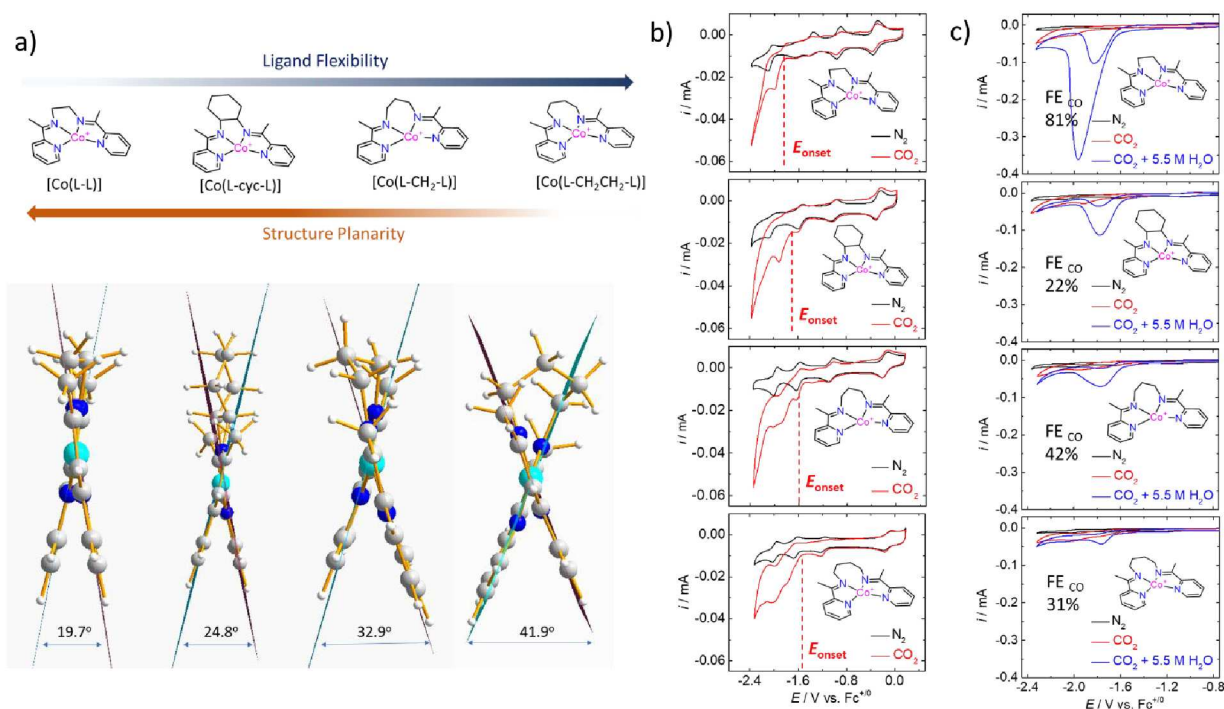


**Figure 17.** a) Systematically altering the flexibility of the aliphatic bridge in the ligand scaffold results in distorts the coordination geometry of the CoN<sub>4</sub> site from a square-planar geometry, as demonstrated by the increased twist angle between two pyridine rings in the ligand scaffold; b) The [Co(L-R-L)] complexes with more flexible ligand scaffolds show only one reversible ligand-based redox feature instead of two stepwise redox features in [Co(L-L)] under N<sub>2</sub>, and operate with more positive  $E_{\text{onset}}$  and slightly increased catalytic current for the CO<sub>2</sub>RR compared to [Co(L-L)] in acetonitrile with trace water (~0.04 M) as the proton source under CO<sub>2</sub>; c) The [Co(L-R-L)] complexes with more flexible ligand scaffolds operate with much lower activity and Faradaic efficiency for CO<sub>2</sub> reduction to CO compared to the rigid [Co(L-L)] in the presence of 5.5 M H<sub>2</sub>O as the proton source. Adapted with permission from *ACS Catal.* **2020**, 10, 9, 4942–4959.<sup>106</sup> Copyright 2020, American Chemical Society.

However, in the presence of the larger concentrations of proton source (5.5 M H<sub>2</sub>O), the [Co(L-R-L)] complexes operate with much lower activity and Faradaic efficiency for CO<sub>2</sub> reduction to CO compared to the rigid [Co(L-L)] (**Figure 17c**). Subsequent experiments suggested that this decreased activity for the CO<sub>2</sub>RR for [Co(L-R-L)] complexes is due to poisoning from the CO product.<sup>106</sup> The more nucleophilic Co centers in the [Co(L-R-L)] complexes more strongly coordinate CO due to increased CO backbonding,<sup>57</sup> leading to the observed product inhibition compared to the [Co(L-L)] with its less nucleophilic Co center.

This Co poisoning was observed only at high concentrations of H<sub>2</sub>O, likely because these conditions enhanced catalytic activity, which in turn increased the local concentration of CO near the catalyst and facilitated CO product inhibition.

This study provided new insights in the design of efficient molecular catalysts that break molecular scaling relationships. Increasing the ligand flexibility of [Co(L-R-L)] was an effective way of preventing catalyst dimerization, and thus shifting catalytic onset to more positive potentials compared to the parent [Co(L-L)] complex. At low concentrations of proton source, the [Co(L-R-L)] complexes also operate with slightly higher activity for the CO<sub>2</sub>RR compared to [Co(L-L)], breaking molecular scaling relationships. However, the increased nucleophilicity of the Co site in the [Co(L-R-L)] structure leads to CO product inhibition not observed in [Co(L-L)] in solutions with large concentrations of proton source. In future studies, incorporating electron-withdrawing substituent into the [Co(L-R-L)] structure may be an effective way to decrease Co site nucleophilicity, prevent CO inhibition, and increase catalytic activity compared to [Co(L-L)] in solutions with high proton source concentration.

## Conclusions

In this perspective, we have discussed challenges of breaking *molecular scaling relationships* in molecular catalysis for the CO<sub>2</sub>RR—the correlation between beneficial decreases in overpotential with detrimental decreases in catalytic activity. We also highlighted and discussed several reported strategies for breaking the molecular scaling relationships from the last decade. Many of these strategies are based on kinetic approaches—stabilizing CO<sub>2</sub>-adduct intermediates to lower the kinetic activation energy barrier  $E_A$  to enhance overall catalytic rate for the CO<sub>2</sub>RR. These include introducing intramolecular electrostatic effects by cationic organic functional groups in the ligand scaffolds or second alkali/alkaline cations in proximity to the active metal center, incorporating proton relays in the secondary coordination sphere to facilitate the delivery of the proton source and stabilize intermediates through created H-bonding networks, and designing binuclear metal complexes where the CO<sub>2</sub> adduct can be coordinated synergistically at two cooperative metal centers. In these scenarios, the catalytic activity of molecular

catalysts is enhanced, but the effective overpotentials usually remain the similar compared to that of the parent complex.

In contrast, breaking the molecular scaling relationship using a thermodynamic approach by modulating the redox potential of the catalytically active species,  $E_{\text{cat}/2}$ , is rare. This is because, for most molecular catalysts, catalytic onset is preceded by a metal-based reduction. Thus,  $E_{\text{cat}/2}$  is correlated to the metal site nucleophilicity—complexes with more positive  $E_{\text{cat}/2}$  tend to have less nucleophilic metal sites, and operate with lower activity for the CO<sub>2</sub>RR.

In the final section in the review, we discussed strategies and progress in our group to break molecular scaling relationships using molecular catalysts with redox active ligands in which the catalytic onset is preceded by a ligand-based reduction rather than a metal-based reduction. In such systems,  $E_{\text{cat}/2}$  and catalytic onset are decoupled from metal site nucleophilicity. Our approach allows us both to tune the electronic structure of the catalyst to decrease effective overpotential (a thermodynamic approach), and to modulate the ability of the ligand to store charge equivalents to enhance the catalytic activity (a kinetic approach).

### Conflicts of Interest

There are no conflicts to declare.

### Acknowledgements

This work was supported by the U.S. Department of Energy, Office of Science, Office of Basic Energy Sciences, Early Career Research Program, under Award DE-SC0022019. W-X. N. acknowledges partial support from a Rackham One-Term Dissertation Fellowship from the University of Michigan.

### Notes and references

1. A. M. Appel, J. E. Bercaw, A. B. Bocarsly, H. Dobbek, D. L. DuBois, M. Dupuis, J. G. Ferry, E. Fujita, R. Hille, P. J. A. Kenis, C. A. Kerfeld, R. H. Morris, C. H. F. Peden, A. R. Portis, S. W. Ragsdale, T. B. Rauchfuss, J. N. H. Reek, L. C. Seefeldt, R. K. Thauer and G. L. Waldrop, *Chem. Rev.*, 2013, **113**, 6621-6658.
2. D. U. Nielsen, X.-M. Hu, K. Daasbjerg and T. Skrydstrup, *Nat. Catal.*, 2018, **1**, 244-254.

3. C. Chen, J. F. Khosrowabadi Kotyk and S. W. Sheehan, *Chem*, 2018, **4**, 2571-2586.
4. P. De Luna, C. Hahn, D. Higgins, S. A. Jaffer, T. F. Jaramillo and E. H. Sargent, *Science*, 2019, **364**, eaav3506.
5. Y. Y. Birdja, E. Pérez-Gallent, M. C. Figueiredo, A. J. Göttle, F. Calle-Vallejo and M. T. M. Koper, *Nat. Energy*, 2019, **4**, 732-745.
6. E. E. Benson, C. P. Kubiak, A. J. Sathrum and J. M. Smieja, *Chem. Soc. Rev.*, 2009, **38**, 89-99.
7. J. Schneider, H. Jia, J. T. Muckerman and E. Fujita, *Chem. Soc. Rev.*, 2012, **41**, 2036-2051.
8. J. Qiao, Y. Liu, F. Hong and J. Zhang, *Chem. Soc. Rev.*, 2014, **43**, 631-675.
9. R. Francke, B. Schille and M. Roemelt, *Chem. Rev.*, 2018, **118**, 4631-4701.
10. C.-F. Leung and P.-Y. Ho, *Catalysts*, 2019, **9**, 760.
11. C. Costentin, M. Robert and J.-M. Saveant, *Chem. Soc. Rev.*, 2013, **42**, 2423-2436.
12. N. Sutin, C. Creutz and E. Fujita, *Comments Inorg. Chem.*, 1997, **19**, 67-92.
13. K. E. Dalle, J. Warnan, J. J. Leung, B. Reuillard, I. S. Karmel and E. Reisner, *Chem. Rev.*, 2019, **119**, 2752-2875.
14. C. W. Li and M. W. Kanan, *J. Am. Chem. Soc.*, 2012, **134**, 7231-7234.
15. K. P. Kuhl, E. R. Cave, D. N. Abram and T. F. Jaramillo, *Energy Environ. Sci.*, 2012, **5**, 7050-7059.
16. Y. Hori, in *Modern Aspects of Electrochemistry*, eds. C. G. Vayenas, R. E. White and M. E. Gamboa-Aldeco, Springer New York, New York, NY, 2008, DOI: 10.1007/978-0-387-49489-0\_3, pp. 89-189.
17. T. Hatsukade, K. P. Kuhl, E. R. Cave, D. N. Abram and T. F. Jaramillo, *Phys. Chem. Chem. Phys.*, 2014, **16**, 13814-13819.
18. Y. Hori, K. Kikuchi and S. Suzuki, *Chem. Lett.*, 1985, **14**, 1695-1698.
19. J. Tafel, *Z. Phys. Chem.*, 1905, **50U**, 641-712.
20. W. Tang, A. A. Peterson, A. S. Varela, Z. P. Jovanov, L. Bech, W. J. Durand, S. Dahl, J. K. Norskov and I. Chorkendorff, *Phys. Chem. Chem. Phys.*, 2012, **14**, 76-81.
21. R. Reske, H. Mistry, F. Behafarid, B. Roldan Cuenya and P. Strasser, *J. Am. Chem. Soc.*, 2014, **136**, 6978-6986.
22. R. Kas, R. Kortlever, A. Milbrat, M. T. Koper, G. Mul and J. Baltrusaitis, *Phys. Chem. Chem. Phys.*, 2014, **16**, 12194-12201.
23. A. S. Hall, Y. Yoon, A. Wuttig and Y. Surendranath, *J. Am. Chem. Soc.*, 2015, **137**, 14834-14837.
24. D. Ren, Y. Deng, A. D. Handoko, C. S. Chen, S. Malkhandi and B. S. Yeo, *ACS Catal.*, 2015, **5**, 2814-2821.
25. Y. Yoon, A. S. Hall and Y. Surendranath, *Angew. Chem. Int. Ed.*, 2016, **55**, 15282-15286.
26. X. Feng, K. Jiang, S. Fan and M. W. Kanan, *ACS Cent. Sci.*, 2016, **2**, 169-174.
27. Y. Li, S. H. Chan and Q. Sun, *Nanoscale*, 2015, **7**, 8663-8683.
28. Y. Wang, P. Han, X. Lv, L. Zhang and G. Zheng, *Joule*, 2018, **2**, 2551-2582.
29. B. Hagman, A. Posada-Borbón, A. Schaefer, M. Shipilin, C. Zhang, L. R. Merte, A. Hellman, E. Lundgren, H. Grönbeck and J. Gustafson, *J. Am. Chem. Soc.*, 2018, **140**, 12974-12979.
30. E. L. Clark, S. Ringe, M. Tang, A. Walton, C. Hahn, T. F. Jaramillo, K. Chan and A. T. Bell, *ACS Catal.*, 2019, **9**, 4006-4014.

31. R. Kas, K. Yang, D. Bohra, R. Kortlever, T. Burdyny and W. A. Smith, *Chem. Sci.*, 2020, **11**, 1738-1749.
32. A. Vasileff, C. Xu, Y. Jiao, Y. Zheng and S.-Z. Qiao, *Chem*, 2018, **4**, 1809-1831.
33. S. Nitopi, E. Bertheussen, S. B. Scott, X. Liu, A. K. Engstfeld, S. Horch, B. Seger, I. E. L. Stephens, K. Chan, C. Hahn, J. K. Nørskov, T. F. Jaramillo and I. Chorkendorff, *Chem. Rev.*, 2019, **119**, 7610-7672.
34. D. J. Martin, C. F. Wise, M. L. Pegis and J. M. Mayer, *Acc. Chem. Res.*, 2020, **53**, 1056-1065.
35. C. Costentin, G. Passard and J.-M. Savéant, *J. Am. Chem. Soc.*, 2015, **137**, 5461-5467.
36. C. Costentin and J.-M. Savéant, *Nature Reviews Chemistry*, 2017, **1**, 0087.
37. S. Fukuzumi, Y.-M. Lee, H. S. Ahn and W. Nam, *Chem. Sci.*, 2018, **9**, 6017-6034.
38. C. Jiang, A. W. Nichols and C. W. Machan, *Dalton Trans.*, 2019, **48**, 9454-9468.
39. N. Corbin, J. Zeng, K. Williams and K. Manthiram, *Nano Research*, 2019, **12**, 2093-2125.
40. Y.-H. Luo, L.-Z. Dong, J. Liu, S.-L. Li and Y.-Q. Lan, *Coord. Chem. Rev.*, 2019, **390**, 86-126.
41. L. Chen, G. Chen, C.-F. Leung, C. Cometto, M. Robert and T.-C. Lau, *Chem. Soc. Rev.*, 2020, **49**, 7271-7283.
42. P. T. Smith, E. M. Nichols, Z. Cao and C. J. Chang, *Acc. Chem. Res.*, 2020, **53**, 575-587.
43. H. S. Shafaat and J. Y. Yang, *Nat. Catal.*, 2021, **4**, 928-933.
44. M. L. Pegis, C. F. Wise, B. Koronkiewicz and J. M. Mayer, *J. Am. Chem. Soc.*, 2017, **139**, 11000-11003.
45. S. Raugei, M. L. Helm, S. Hammes-Schiffer, A. M. Appel, M. O'Hagan, E. S. Wiedner and R. M. Bullock, *Inorg. Chem.*, 2016, **55**, 445-460.
46. A. Dutta, B. Ginovska, S. Raugei, J. A. S. Roberts and W. J. Shaw, *Dalton Trans.*, 2016, **45**, 9786-9793.
47. A. J. P. Cardenas, B. Ginovska, N. Kumar, J. Hou, S. Raugei, M. L. Helm, A. M. Appel, R. M. Bullock and M. O'Hagan, *Angew. Chem. Int. Ed.*, 2016, **55**, 13509-13513.
48. M. L. Pegis, B. A. McKeown, N. Kumar, K. Lang, D. J. Wasylenko, X. P. Zhang, S. Raugei and J. M. Mayer, *ACS Cent. Sci.*, 2016, **2**, 850-856.
49. I. Azcarate, C. Costentin, M. Robert and J.-M. Savéant, *J. Phys. Chem. C*, 2016, **120**, 28951-28960.
50. M. L. Clark, P. L. Cheung, M. Lessio, E. A. Carter and C. P. Kubiak, *ACS Catal.*, 2018, **8**, 2021-2029.
51. S. E. Tignor, H.-Y. Kuo, T. S. Lee, G. D. Scholes and A. B. Bocarsly, *Organometallics*, 2019, **38**, 1292-1299.
52. B. M. Ceballos and J. Y. Yang, *Proc. Natl. Acad. Sci. U.S.A.*, 2018, **115**, 12686-12691.
53. J. M. Barlow and J. Y. Yang, *ACS Cent. Sci.*, 2019, DOI: 10.1021/acscentsci.9b00095.
54. X. Liu, J. Xiao, H. Peng, X. Hong, K. Chan and J. K. Nørskov, *Nat. Commun.*, 2017, **8**, 15438.
55. J. M. Barlow and J. Y. Yang, *ACS Cent. Sci.*, 2019, **5**, 580-588.
56. M. H. Schmidt, G. M. Miskelly and N. S. Lewis, *J. Am. Chem. Soc.*, 1990, **112**, 3420-3426.
57. E. Fujita, C. Creutz, N. Sutin and D. J. Szalda, *J. Am. Chem. Soc.*, 1991, **113**, 343-353.
58. T. Ogata, S. Yanagida, B. S. Brunschwig and E. Fujita, *J. Am. Chem. Soc.*, 1995, **117**, 6708-6716.
59. M. L. Pegis, J. A. S. Roberts, D. J. Wasylenko, E. A. Mader, A. M. Appel and J. M. Mayer, *Inorg. Chem.*, 2015, **54**, 11883-11888.
60. Y. Matsubara, *ACS Energy Lett.*, 2017, **2**, 1886-1891.

61. N. Elgrishi, M. B. Chambers, X. Wang and M. Fontecave, *Chem. Soc. Rev.*, 2017, **46**, 761-796.
62. B. Sawatlon, M. D. Wodrich and C. Corminboeuf, *Organometallics*, 2018, **37**, 4568-4575.
63. Y.-H. Wang, P. E. Schneider, Z. K. Goldsmith, B. Mondal, S. Hammes-Schiffer and S. S. Stahl, *ACS Cent. Sci.*, 2019, **5**, 1024-1034.
64. M. L. Helm, M. P. Stewart, R. M. Bullock, M. R. DuBois and D. L. DuBois, *Science*, 2011, **333**, 863-866.
65. C. Costentin, S. Drouet, M. Robert and J.-M. Savéant, *Science*, 2012, **338**, 90-94.
66. S. Sung, D. Kumar, M. Gil-Sepulcre and M. Nippe, *J. Am. Chem. Soc.*, 2017, **139**, 13993-13996.
67. A. Chapovetsky, T. H. Do, R. Haiges, M. K. Takase and S. C. Marinescu, *J. Am. Chem. Soc.*, 2016, **138**, 5765-5768.
68. S. Roy, B. Sharma, J. Pécaut, P. Simon, M. Fontecave, P. D. Tran, E. Derat and V. Artero, *J. Am. Chem. Soc.*, 2017, **139**, 3685-3696.
69. Eva M. Nichols, J. S. Derrick, S. K. Nistanaki, P. T. Smith and C. J. Chang, *Chem. Sci.*, 2018, **9**, 2952-2960.
70. A. Chapovetsky, M. Welborn, J. M. Luna, R. Haiges, T. F. Miller and S. C. Marinescu, *ACS Cent. Sci.*, 2018, **4**, 397-404.
71. P. Gotico, B. Boitrel, R. Guillot, M. Sircoglou, A. Quaranta, Z. Halime, W. Leibl and A. Aukauloo, *Angew. Chem. Int. Ed.*, 2019, **58**, 4504-4509.
72. C. G. Margarit, C. Schnedermann, N. G. Asimow and D. G. Nocera, *Organometallics*, 2019, **38**, 1219-1223.
73. I. Azcarate, C. Costentin, M. Robert and J.-M. Savéant, *J. Am. Chem. Soc.*, 2016, **138**, 16639-16644.
74. C. Costentin, S. Drouet, M. Robert and J.-M. Savéant, *J. Am. Chem. Soc.*, 2012, **134**, 11235-11242.
75. J. A. S. Roberts and R. M. Bullock, *Inorg. Chem.*, 2013, **52**, 3823-3835.
76. E. S. Rountree, B. D. McCarthy, T. T. Eisenhart and J. L. Dempsey, *Inorg. Chem.*, 2014, **53**, 9983-10002.
77. K. J. Lee, N. Elgrishi, B. Kandemir and J. L. Dempsey, *Nature Reviews Chemistry*, 2017, **1**, 0039.
78. V. C. C. Wang and B. A. Johnson, *ACS Catal.*, 2019, DOI: 10.1021/acscatal.9b00850, 7109-7123.
79. K. J. Lee, B. D. McCarthy and J. L. Dempsey, *Chem. Soc. Rev.*, 2019, **48**, 2927-2945.
80. H. A. Hansen, J. B. Varley, A. A. Peterson and J. K. Nørskov, *J. Phys. Chem. Lett.*, 2013, **4**, 388-392.
81. A. H. Reath, J. W. Ziller, C. Tsay, A. J. Ryan and J. Y. Yang, *Inorg. Chem.*, 2017, **56**, 3713-3718.
82. T. Chantarojsiri, J. W. Ziller and J. Y. Yang, *Chem. Sci.*, 2018, **9**, 2567-2574.
83. T. Chantarojsiri, A. H. Reath and J. Y. Yang, *Angew. Chem. Int. Ed.*, 2018, **57**, 14037-14042.
84. K. Kang, J. Fuller, A. H. Reath, J. W. Ziller, A. N. Alexandrova and J. Y. Yang, *Chem. Sci.*, 2019, **10**, 10135-10142.
85. A. Parkin, J. Seravalli, K. A. Vincent, S. W. Ragsdale and F. A. Armstrong, *J. Am. Chem. Soc.*, 2007, **129**, 10328-10329.
86. J.-H. Jeoung and H. Dobbek, *Science*, 2007, **318**, 1461-1464.
87. S. Lense, K. A. Grice, K. Gillette, L. M. Wolf, G. Robertson, D. McKeon, C. Saucedo, P. J. Carroll and M. Gau, *Organometallics*, 2020, **39**, 2425-2437.
88. J. Agarwal, T. W. Shaw, H. F. Schaefer and A. B. Bocarsly, *Inorg. Chem.*, 2015, **54**, 5285-5294.

89. K. T. Ngo, M. McKinnon, B. Mahanti, R. Narayanan, D. C. Grills, M. Z. Ertem and J. Rochford, *J. Am. Chem. Soc.*, 2017, **139**, 2604-2618.
90. A. W. Nichols, S. L. Hooe, J. S. Kuehner, D. A. Dickie and C. W. Machan, *Inorg. Chem.*, 2020, **59**, 5854-5864.
91. M. H. Rønne, D. Cho, M. R. Madsen, J. B. Jakobsen, S. Eom, É. Escoudé, H. C. D. Hammershøj, D. U. Nielsen, S. U. Pedersen, M.-H. Baik, T. Skrydstrup and K. Daasbjerg, *J. Am. Chem. Soc.*, 2020, **142**, 4265-4275.
92. M. R. Madsen, J. B. Jakobsen, M. H. Rønne, H. Liang, H. C. D. Hammershøj, P. Nørby, S. U. Pedersen, T. Skrydstrup and K. Daasbjerg, *Organometallics*, 2020, **39**, 1480-1490.
93. S. Sung, X. Li, L. M. Wolf, J. R. Meeder, N. S. Bhuvanesh, K. A. Grice, J. A. Panetier and M. Nippe, *J. Am. Chem. Soc.*, 2019, **141**, 6569-6582.
94. E. Haviv, D. Azaiza-Dabbah, R. Carmieli, L. Avram, J. M. L. Martin and R. Neumann, *J. Am. Chem. Soc.*, 2018, **140**, 12451-12456.
95. D. Z. Zee, M. Nippe, A. E. King, C. J. Chang and J. R. Long, *Inorg. Chem.*, 2020, **59**, 5206-5217.
96. T. Ouyang, H.-H. Huang, J.-W. Wang, D.-C. Zhong and T.-B. Lu, *Angew. Chem. Int. Ed.*, 2017, **56**, 738-743.
97. T. Ouyang, H.-J. Wang, H.-H. Huang, J.-W. Wang, S. Guo, W.-J. Liu, D.-C. Zhong and T.-B. Lu, *Angew. Chem. Int. Ed.*, 2018, **57**, 16480-16485.
98. L.-M. Cao, H.-H. Huang, J.-W. Wang, D.-C. Zhong and T.-B. Lu, *Green Chem.*, 2018, **20**, 798-803.
99. Z. Guo, G. Chen, C. Cometto, B. Ma, H. Zhao, T. Groizard, L. Chen, H. Fan, W.-L. Man, S.-M. Yiu, K.-C. Lau, T.-C. Lau and M. Robert, *Nat. Catal.*, 2019, **2**, 801-808.
100. Q. Knijnenburg, S. Gambarotta and P. H. M. Budzelaar, *Dalton Trans.*, 2006, DOI: 10.1039/B612251E, 5442-5448.
101. B. de Bruin, E. Bill, E. Bothe, T. Weyhermüller and K. Wieghardt, *Inorg. Chem.*, 2000, **39**, 2936-2947.
102. D. C. Lacy, C. C. L. McCrory and J. C. Peters, *Inorg. Chem.*, 2014, **53**, 4980-4988.
103. M. Zhang, M. El-Roz, H. Frei, J. L. Mendoza-Cortes, M. Head-Gordon, D. C. Lacy and J. C. Peters, *J. Phys. Chem. C*, 2015, **119**, 4645-4654.
104. W. Nie, D. E. Tarnopol and C. C. L. McCrory, *J. Am. Chem. Soc.*, 2021, **143**, 3764-3778.
105. W. Nie and C. C. L. McCrory, *Chem. Commun.*, 2018, **54**, 1579-1582.
106. W. Nie, Y. Wang, T. Zheng, A. Ibrahim, Z. Xu and C. C. L. McCrory, *ACS Catal.*, 2020, **10**, 4942-4959.

## Photographs and Biographies



Weixuan Nie obtained his B.S. and M.S. degrees in Chemistry from Nanjing University, P.R. China. He earned his Ph.D. from the University of Michigan in 2021, where he worked with Prof. Charles C. L. McCrory to design novel molecular catalysts for electrochemical CO<sub>2</sub> reduction. He is currently a postdoctoral research with Prof. Jonas C. Peters and Prof. Theodor Agapie at the California Institute of Technology as part of the Liquid Sunlight Alliance (LiSA), an Energy Innovation Hub of the U.S. Department of Energy. His current research focuses on (photo)electrochemical CO<sub>2</sub> reduction to value-added liquid C<sub>2-2</sub> products by solid-state catalyst systems.



Charles C. L. McCrory earned his Ph.D. in Chemistry from Stanford University in 2010 under the guidance of Prof. Christopher E. D. Chidsey, and conducted postdoctoral research with Prof. Jonas C. Peters at the California Institute of Technology. From 2011-2015, he was a senior scientist at the Joint Center for Artificial Synthesis (JCAP), an Energy Innovation Hub of the U.S. Department of Energy. He is currently an Assistant Professor of Chemistry and Assistant Professor of Macromolecular Science & Engineering at the University of Michigan, where his group studies the mechanisms and kinetics of electrocatalysis for energy storage and environmental remediation.